













Signatures of Dipolarizing Flux Bundles in the Nightside Auroral Zone

Mark J. Engebretson¹ , Sean A. Gaffaney¹ , Jesus A. Ochoa¹, Andrei Runov² , James M. Weygand² , Yukitoshi Nishimura³ , Michael D. Hartinger^{2,4} , Vyacheslav A. Pilipenko⁵ , Mark B. Moldwin⁶ , Martin G. Connors⁷ , Ian R. Mann⁸ , Zhonghua Xu⁹ , and Juan V. Rodriguez^{10,11} 

¹Department of Physics, Augsburg University, Minneapolis, MN, USA, ²UCLA Department of Earth Planetary and Space Sciences, Los Angeles, CA, USA, ³Department of Electrical and Computer Engineering and Center for Space Physics, Boston University, Boston, MA, USA, ⁴Space Science Institute, Boulder, CO, USA, ⁵Space Research Institute, Moscow, Russian Federation, ⁶Department of Climate and Space Sciences and Engineering, University of Michigan, Ann Arbor, MI, USA, ⁷Athabasca University Observatories, Athabasca University, Athabasca, AB, USA, ⁸Department of Physics, University of Alberta, Edmonton, AB, USA, ⁹Department of Electrical and Computer Engineering, Virginia Tech, Hampton, VA, USA, ¹⁰Cooperative Institute for Research in Environmental Sciences, University of Colorado Boulder, Boulder, CO, USA, ¹¹NOAA National Centers for Environmental Information, Boulder, CO, USA

Key Points:

- Geomagnetic disturbances observed in ground magnetometer data can coincide with dipolarizing flux bundles observed by THEMIS spacecraft
- Coincident isolated premidnight GMDs and DFBs are strongly associated with high solar wind velocity but not with geomagnetic storms
- Isolated premidnight DFBs generated under these conditions trigger only highly localized and transient upward currents and auroras

Supporting Information:

Supporting Information may be found in the online version of this article.

Correspondence to:

M. J. Engebretson,
engebret@augsborg.edu

Citation:

Engebretson, M. J., Gaffaney, S. A., Ochoa, J. A., Runov, A., Weygand, J. M., Nishimura, Y., et al. (2024). Signatures of dipolarizing flux bundles in the nightside auroral zone. *Journal of Geophysical Research: Space Physics*, 129, e2023JA032266. <https://doi.org/10.1029/2023JA032266>

Received 7 NOV 2023

Accepted 11 MAR 2024

Author Contributions:

Conceptualization: Mark J. Engebretson, Andrei Runov, Yukitoshi Nishimura, Michael D. Hartinger, Vyacheslav A. Pilipenko

Data curation: Mark J. Engebretson, Yukitoshi Nishimura, Mark B. Moldwin, Martin G. Connors, Ian R. Mann, Juan V. Rodriguez

Formal analysis: Mark J. Engebretson, Andrei Runov, James M. Weygand, Yukitoshi Nishimura

Funding acquisition: Mark J. Engebretson

Investigation: Mark J. Engebretson, Sean A. Gaffaney, Jesus A. Ochoa,

Andrei Runov, James M. Weygand, Yukitoshi Nishimura, Zhonghua Xu

Methodology: Mark J. Engebretson, Andrei Runov, James M. Weygand, Yukitoshi Nishimura

Abstract Dipolarizing flux bundles (DFBs) have been suggested to transport energy and momentum from regions of reconnection in the magnetotail to the high latitude ionosphere, where they can generate localized ionospheric currents that can produce large nighttime geomagnetic disturbances (GMDs). In this study we identified DFBs observed in the midnight sector from ~ 7 to $\sim 10 R_E$ by THEMIS A, D, and E during days in 2015–2017 whose northern hemisphere magnetic footpoints mapped to regions near Hudson Bay, Canada, and have compared them to isolated GMDs observed by ground magnetometers. We found 6 days during which one or more of these DFBs coincided to within ± 3 min with ≥ 6 nT/s GMDs observed by latitudinally closely spaced ground-based magnetometers located near those footpoints. Spherical elementary current systems (SECS) maps and all-sky imager data provided further characterization of two events, showing short-lived localized intense upward currents, auroral intensifications and/or streamers, and vortical perturbations of a westward electrojet. On all but one of these days the coincident DFB—GMD pairs occurred during intervals of high-speed solar wind streams but low values of SYM/H. The observations reported here indicate that isolated DFBs generated under these conditions influence only limited spatial regions nearer Earth. In some events, in which the DFBs were observed closer to Earth and with lower Earthward velocities, the GMDs occurred slightly earlier than the DFBs, suggesting that braking had begun before the time of the DFB observation.

1. Introduction

Dipolarizing flux bundles (DFBs) are defined observationally as transient (~ 1 min) magnetotail flux tubes (usually with diameters $< \sim 3 R_E$ in XGSM and YGSM coordinates) with a significantly more dipolar (northward) magnetic field than their background and with a density lower than the surrounding plasma. They typically propagate Earthward at high speed, ~ 300 km/s, but in individual events up to 500–800 km/s (Runov et al., 2009, 2011) from a reconnection site deeper in the magnetotail (Liu, Angelopoulos, Runov, & Zhou, 2013; Liu et al., 2014; Nagai et al., 1998; Petrukovich et al., 1998) and eventually stop near the inner edge of the plasma sheet (Dubyaagin et al., 2010; Liu et al., 2017; Shiokawa et al., 1997). They are enveloped in larger 10 min time scale Earthward-moving bursty bulk flows (BBFs, as originally identified by Baumjohann et al. (1989, 1990) and Angelopoulos et al. (1992, 1994) and further characterized by Angelopoulos et al. (1996), Sergeev et al. (1996), and Nakamura et al. (2004). Dipolarization fronts, ion gyro-scale boundaries separating the plasma inside a DFB from the ambient plasma sheet and characterized by a small amplitude negative B_z variation followed by a sharp increase in B_z of \sim tens of nT, are often observed at the leading edge of BBFs (Ohtani et al., 2004; Runov et al., 2012). The time that such an increase in B_z is observed is used as the time of the DFB (Liu, Angelopoulos, Runov, & Zhou, 2013).

Both the ion pressure and bulk velocity are observed to increase about 1 min before dipolarization front crossings (e.g., Figures 5 and 6 of Runov et al., 2011). Zhou et al. (2010, 2011) noted that an earthward streaming ion population increased as the dipolarization front moved nearer to Earth, and test particle simulations showed that this

observed ion distribution was consistent with a picture of ions reflected and accelerated by the approaching front, and suggested that the incoming front could be decelerated by these reflected ions. Li et al. (2011) suggested a complementary picture in that a pressure gradient ahead of the front could be built up by the streaming population, which might result in acceleration of the ambient plasma without direct interaction with the dipolarization front.

The impact of BBFs on the ionosphere was studied by Kauristie et al. (1996), who identified isolated plasma sheet bubbles observed by the AMPTE/IRM satellite while its magnetic footprint was close to the EISCAT Magnetometer Cross. They found that in most cases the magnetic field observations were consistent with Hall current vortices forming in the ionosphere at the footprint of localized field-aligned currents. An event study by Runov et al. (2011) showed that a DFB impacting the near-Earth transition region led to the formation of a system of field-aligned currents that reached the ionosphere (e.g., Birn et al., 2019; Sergeev et al., 2014). FAC closure through intensified westward electrojet currents resulted in perturbations in the geomagnetic field observed by ground-based magnetometers (McPherron et al., 1973) and the formation of a north-south auroral form, as reported also in earlier studies (Nakamura, Baumjohann, Schödel, et al., 2001; Sergeev, Sauvaud, Popescu, Kovrazhkin, Liou, et al., 2000; Sergeev, Sauvaud, Popescu, Kovrazhkin, Lutsenko, et al., 2000) and documented in recent reviews (Forsyth et al., 2020; Lyons et al., 2022).

Much of the focus on BBFs and DFBs has been on the impact of a series of these events during or preceding substorms (e.g., Liu, Angelopoulos, Runov, & Zhou, 2013). Much less attention has been paid to the presence and impact of isolated BBF/DFB events as possible drivers of large, isolated nighttime geomagnetic disturbances (GMDs), also known as magnetic perturbation events (MPEs).

However, Wei et al. (2021) combined BBF data from Cluster, field-aligned current data from the low-altitude Swarm satellites, and observations of a train of GMDs from seven stations in central Canada for an interval during the 7 January 2015 geomagnetic storm, and provided direct evidence that a wide range of intense dB/dt variations was associated with a large-scale substorm current system, driven by multiple BBFs.

An earlier study by Jusuola et al. (2009), however, found both similarities and differences between the ionospheric equivalent currents (the changes of which can generate GMDs) associated with BBFs during both substorm and nonsubstorm conditions. Of 134 conjunctions identified between Cluster observations of BBFs on magnetic field lines that mapped to the IMAGE magnetometer array in Scandinavia, Jusuola et al. (2009) identified 18 that contained one or more BBFs, nine during substorms and nine during nonsubstorm conditions. In 16 of the 18 conjunctions, BBFs were associated with an intensification of a southeast-northwest aligned narrow channel of enhanced northwestward equivalent current density, with downward field-aligned current at its northeastward flank and upward field-aligned current at its southwestward flank. During substorm BBFs the channel was generally superposed on a relatively disturbed background including the substorm electrojet. A superposed epoch analysis of the local IMAGE AE (IE) index revealed a stronger activity level preceding a substorm-related BBF than a nonsubstorm BBF. After the BBF observation, however, the activity in both cases was on the same level as that preceding the substorm BBF observation. Jusuola et al. (2009) also cited the observations of Nakamura, Baumjohann, Brittnacher, et al. (2001), who noted that two main kinds of auroral signatures have been observed during BBFs: pseudobreakups and auroral streamers. Pseudobreakups appear in auroral images as a bright spot that may last only a few minutes and then fade, or brighten intermittently, while auroral streamers are approximately north-south aligned and longitudinally narrow auroral forms that first appear at the poleward boundary of the auroral oval and from there expand equatorward.

More recently, Panov, Baumjohann, Nakamura, Pritchett, et al. (2019) compared observations of DFBs that were observed by THEMIS spacecraft during non-substorm times amidst azimuthally drifting interchange heads (depleted plasma tubes) in the near magnetotail to observations by magnetically conjugate all-sky images and magnetometer networks near THEMIS magnetic footprints. Although this study focused on the association of interchange heads with DFBs, it also showed that localized and short-lived intensifications of up/down current pairs, westward electrojet currents, and auroral bright spots occurred near THEMIS footprints during each DFB. Both the Jusuola et al. (2009) and Panov, Baumjohann, Nakamura, Pritchett, et al. (2019) studies observed features consistent with those reported here, but neither study made explicit connections to occurrences of GMDs.

What is new about this current study is its detailed temporal focus on large, localized, and isolated geomagnetic disturbances (GMDs) at auroral zone latitudes that often have amplitudes >6 nT/s (>360 nT/min), and thus are capable of exciting bursts of geomagnetically induced currents (GICs) in susceptible infrastructure (Engebretson,

Pilipenko, et al., 2019; Engebretson, Steinmetz, et al., 2019; Engebretson, Pilipenko, et al., 2021; Engebretson, Ahmed, et al., 2021; Weygand et al., 2021). The introduction of Zou et al. (2022) provides a review of the several varieties of auroras that are associated with large dB/dt events, including spatially localized ones. Engebretson, Steinmetz, et al. (2019) and Weygand et al. (2021) showed examples of localized GMDs that were accompanied by localized equivalent ionospheric currents, localized pairs of upward/downward vertical currents (proxies for field-aligned currents), and often poleward boundary intensifications and/or auroral streamers. Engebretson, Pilipenko, et al. (2019) and Engebretson, Steinmetz, et al. (2019) found that the horizontal half-amplitude radius of these GMDs was ~ 275 km, and Weygand et al. (2021) reported a range of ~ 250 – 450 km for several events, with a somewhat greater longitudinal extent in some cases.

Section 2 describes the data set of DFBs and the ground magnetometers with whose data they are compared. Section 3 presents detailed case studies of intervals on 2 days that also include all-sky auroral imager data and maps of equivalent ionospheric and vertical currents over North America produced using the spherical elementary currents (SECS) method. Section 4 provides detailed timing and geophysical context information for DFB-GMD events during 6 days that occurred within ± 3 min of each other. Composite figures showing the time series of the DFBs and GMDs during the other 4 days are provided in Supporting Information S1. Section 5 discusses some of the challenges in identifying these events and the implications of their relative timing, and Section 6 summarizes our findings.

2. Instrumentation and Data Set

The Time History of Events and Macroscale Interactions during Substorms (THEMIS) set of five spacecraft were launched in 2007 into highly elliptical orbits with apogees of 10, 12, 12, 20, and 30 R_E (Angelopoulos, 2008; Sibeck & Angelopoulos, 2008). In 2010 the two spacecraft with the highest apogee were moved into lunar orbit and comprise the Acceleration, Reconnection, Turbulence and Electrodynamics of Moon's Interaction with the Sun (ARTEMIS) mission, and the apogees of the other three spacecraft have been fixed at $\sim 12 R_E$ in orbits separated by approximately 500–3,000 km.

The Fluxgate Magnetometer (FGM) instrument on the THEMIS spacecraft (Auster et al., 2008) provides DC magnetic field measurements with a temporal resolution of 128 vectors per second during the burst mode. The Electrostatic Analyzer (ESA) (McFadden et al., 2008) provides ion and electron distribution functions in the 5 eV to 25 keV energy range with a time resolution of one 3-D distribution function per spin in the burst mode. The Solid State Telescope (SST) (Angelopoulos, 2008) detects high-energy (30 keV–1 MeV) ion and electron fluxes with a time resolution of one 3-D distribution function per spin in the burst and reduced modes.

The Magnetospheric Electron Detector (MAGED) and Magnetospheric Proton Detector (MAGPD) on GOES 13–15 in geostationary orbit measure 30–600 keV electron fluxes and 80–800 keV proton fluxes, respectively, in five energy bands (Hanser, 2011). Each instrument consisted of nine identical-design telescopes in a cruciform arrangement (Sillanpää et al., 2017). Co-manifested with MAGED and MAGPD were a pair of fluxgate magnetometers (inboard and outboard) on a boom (Califf et al., 2023). Pitch angles for MAGED and MAGPD are calculated from the magnetic field vectors measured by the outboard magnetometer.

Ground-based magnetometer data used in this study were recorded by stations in the MACCS (Engebretson et al., 1995), AUTUMNX (Connors et al., 2016), CARISMA (Mann et al., 2008), CANMOS (Nikitina et al., 2016), and THEMIS GBO (Russell et al., 2008) arrays in Arctic Canada, as detailed in Table 1 and Figure 1 (red circles). Figure 1 shows the locations of the magnetometers in the Hudson Bay region that have been used in this study, as well as the northern hemisphere magnetic field footpoints of geostationary spacecraft GOES 13 and 14. Table 1 lists the locations of these magnetometers in geographic and geomagnetic coordinates, and Table 2 lists the geographic distances between the stations located in two latitudinal chains along the west and east coasts of Hudson Bay, respectively. The sampling cadence of these instruments, 1.0 or 0.5 s, permits viewing the full detail of the GMDs reported here, including their derivative amplitudes (e.g., the several examples comparing time series with these cadences to down-sampled 1-min data shown by Zou et al. (2022)).

This study also makes use of all-sky white-light images produced by THEMIS imagers located at RANK and Fort Smith (Donovan et al., 2006; Mende et al., 2008), 630.0 nm all-sky images produced by the Redline Emission Geospace Observatory (REGO) imager at TPAS, each presented at a 15-s cadence, and maps of equivalent ionospheric and vertical currents (a proxy for field-aligned currents) over North America produced using the

Table 1
Ground-Based Magnetometers Used in This Study

Array	Station	Code	Geog. Lat.	Geog. Lon.	CGM Lat.	CGM Lon.	Cadence
MACCS	Cape Dorset	CDR	64.2°	283.4°	72.6°	2.8°	0.5 s
AUTUMNX	Salluit	SALU	62.2°	284.4°	70.6°	4.1°	0.5 s
	Puvurmituq	PUVR	60.0°	282.7°	68.7°	1.2°	0.5 s
	Inukjuak	INUK	58.5°	281.9°	67.4°	0.0°	0.5 s
	Kuujuarapik	KJPK	55.3°	282.3°	64.3°	0.3°	0.5 s
CANMOS	Baker Lake	BLC	64.3°	263.9°	72.7°	29.0°	1.0 s
	Sanikiluaq	SNK	56.5°	280.8°	65.5°	-1.9°	1.0 s
CARISMA	Rankin Inlet	RANK	62.8°	267.9°	71.6°	-22.2°	1.0 s
	Fort Churchill	FCHU	58.8°	265.9°	67.8°	-24.8°	1.0 s
	Back Lake	BACK	57.7°	265.8°	66.8°	-24.8°	1.0 s
	Gillam	GILL	56.4°	265.4°	65.5°	-25.3°	1.0 s
	Rabbit Lake	RABB	58.2°	256.3°	66.3°	-39.0°	1.0 s
THEMIS	The Pas	TPAS	54.0°	259.1°	62.5°	-34.2°	0.5 s

Note. Corrected magnetic (CGM) coordinates are for 1 January 2017 using http://sdnet.thayer.dartmouth.edu/aacgm/aacgm_calc.php#AACGM.

Spherical Elementary Current Systems (SECS) technique (Amm & Viljanen, 1999; Weygand, 2009a, 2009b; Weygand et al., 2011), presented at a 30-s cadence.

Our study focuses on DFBs observed by THEMIS A, D, and E during 2015, 2016, and 2017, the 3 years during the solar cycle that coincided with the largest number of ≥ 6 nT/s GMDs identified during solar cycle 24 in observations by several MACCS magnetometers in eastern Arctic Canada (Engebretson et al., 2024). Candidate events

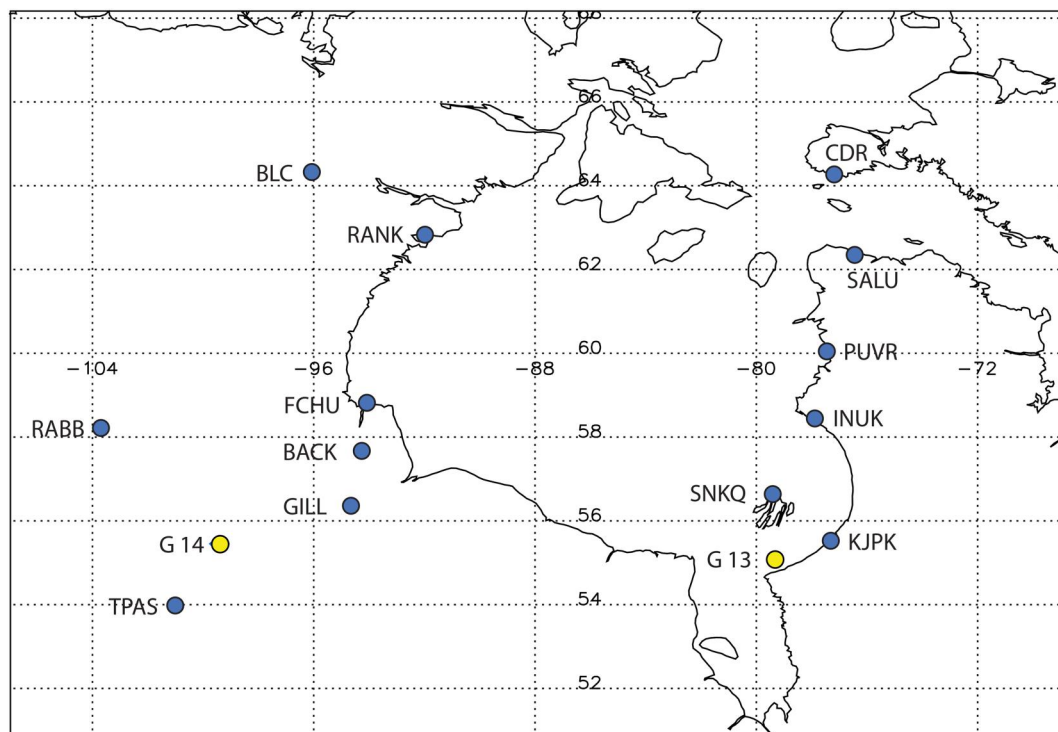


Figure 1. Map of the Hudson Bay region in Arctic Canada showing ground magnetometer stations used for this study (blue circles) and the magnetic footprints of GOES 13 and 14 at 0600 UT 27 January 2017 (yellow circles).

Table 2
Geographic Distances Between Adjacent Pairs of Magnetometer Stations Along the West and East Coast of Hudson Bay, Respectively

Station pair	Distance (km)	Station pair	Distance (km)
RANK—FCHU	458	CDR—SALU	228
FCHU—BACK	123	SALU—PUVR	261
BACK—GILL	147	PUVR—INUK	173
RABB—BACK	562	INUK—KJPK	356
		KJPK - RADI	167

on 198 days satisfied two initial criteria: they were observed during passes over the North American continent, and their $\sim 12 R_E$ apogees were within ~ 3 hr MLT of local midnight. The NASA SSCWEB utility was then used to display approximate mappings of the northern hemisphere footpoints of the magnetic field line through the relevant THEMIS spacecraft of candidate events in order to identify events that mapped to the region from west of Hudson Bay to east of Hudson Bay shown in Figure 1. Each event during the resulting 48 days was compared to ground magnetometer data from the stations near the east and west coasts of Hudson Bay shown in Figure 1. Events during which the DFBs mapped to the center of Hudson Bay typically produced little or weak GMD activity at the magnetometer sites on either the

west or east coast, and were excluded from further consideration. Events with temporally overlapping DFBs were also excluded regardless of the presence of large GMDs. However, during six of these days one or more clear and isolated DFBs occurred within ± 3 min of GMDs at one or more of these stations.

3. Example Events

Two events will be presented in detail in this section; on both days all-sky auroral images were available before, during, and after nearly simultaneous DFBs and GMDs.

3.1. 27 January 2017

On this day two GMDs occurred within ~ 15 min of each other while THEMIS D and THEMIS-E were nearly overhead of the FCHU-BACK-GILL chain of magnetometers near the southwestern edge of Hudson Bay. No DFBs were identified by THEMIS spacecraft later on 27 January 2017, when their footpoints were located progressively farther west.

Figure 2 shows a summary plot of THEMIS D observations between 05:20 and 06:20 UT on 27 January 2017. Shown are magnetic field components (panel a), electron and ion time-energy spectrograms (panels b and c), ion density (panel d), ion and electron temperatures (panel e), and ion bulk velocity (panel f). It is evident from these observations that prior to the plasma sheet expansion at 05:45 UT, associated with a decrease in the magnetic field strength due mainly to B_x becoming smaller in magnitude, the density and temperature increased, and with enhancement in the ion bulk flow, THEMIS D was at the plasma sheet boundary layer south of the neutral sheet (as evidenced by the negative magnetic field component B_x). Weak signatures of DFBs were observed shortly thereafter, at 05:46:58 and 05:48:20 UT. Notably, the B_x magnitude reached 70.5 nT and then dropped to 30 nT during the plasma expansion. It is also worthy of note that although energies of both ions and electrons increased during the plasma sheet expansion, the increase in the electron energy was larger than that of the ions. Immediately after the expansion associated with a distinct magnetic field structure, characterized by a B_z jump, sharp B_y rotation, and drop in $|B_x|$, THEMIS D started to detect a significant energy flux of electrons at energies up to 100 keV. Correspondingly, the electron temperature increased during the expansion from ~ 100 eV to ~ 5 keV and became comparable with the ion temperature, which increased at the same time.

A later, more distinct DFB was detected by THEMIS D at 05:59:23 UT. It was associated with a brief drop in the density and an enhancement in the ion bulk velocity in the sunward direction ($V_x > 0$). THEMIS D also detected electron injections at energies exceeding 100 keV. The electron temperature increased again up to ~ 5 keV and became close to the ion temperature. A similar plot of THEMIS E data (not shown) revealed no evidence of the first DFB, but signatures similar to those of the second DFB at 06:01 UT.

Figure 3 shows IMF and solar wind data from the OMNI data base, time-shifted to the nose of the bow shock, as well as three magnetic activity indices (AL , AU , and SYM/H) from 05:20 to 06:20 UT on this day. The times of the DFBs observed by THEMIS D and E are indicated by vertical red lines. The two shaded regions indicate time intervals with nearly simultaneous GMDs observed by five ground magnetometers located along the west coast of Hudson Bay. Each region is also highlighted in Figures 4 and 5, and will be examined in greater detail in Figures 6–8.

During the period shown in Figure 3 and during both shaded intervals the IMF B_x component (panel a) was negative and the B_y component (panel b) was positive. The B_z component (panel c) was mostly near 0 nT before the first shaded interval and rose to +7 nT near 05:45 UT, shortly before the first DFB. It remained positive during

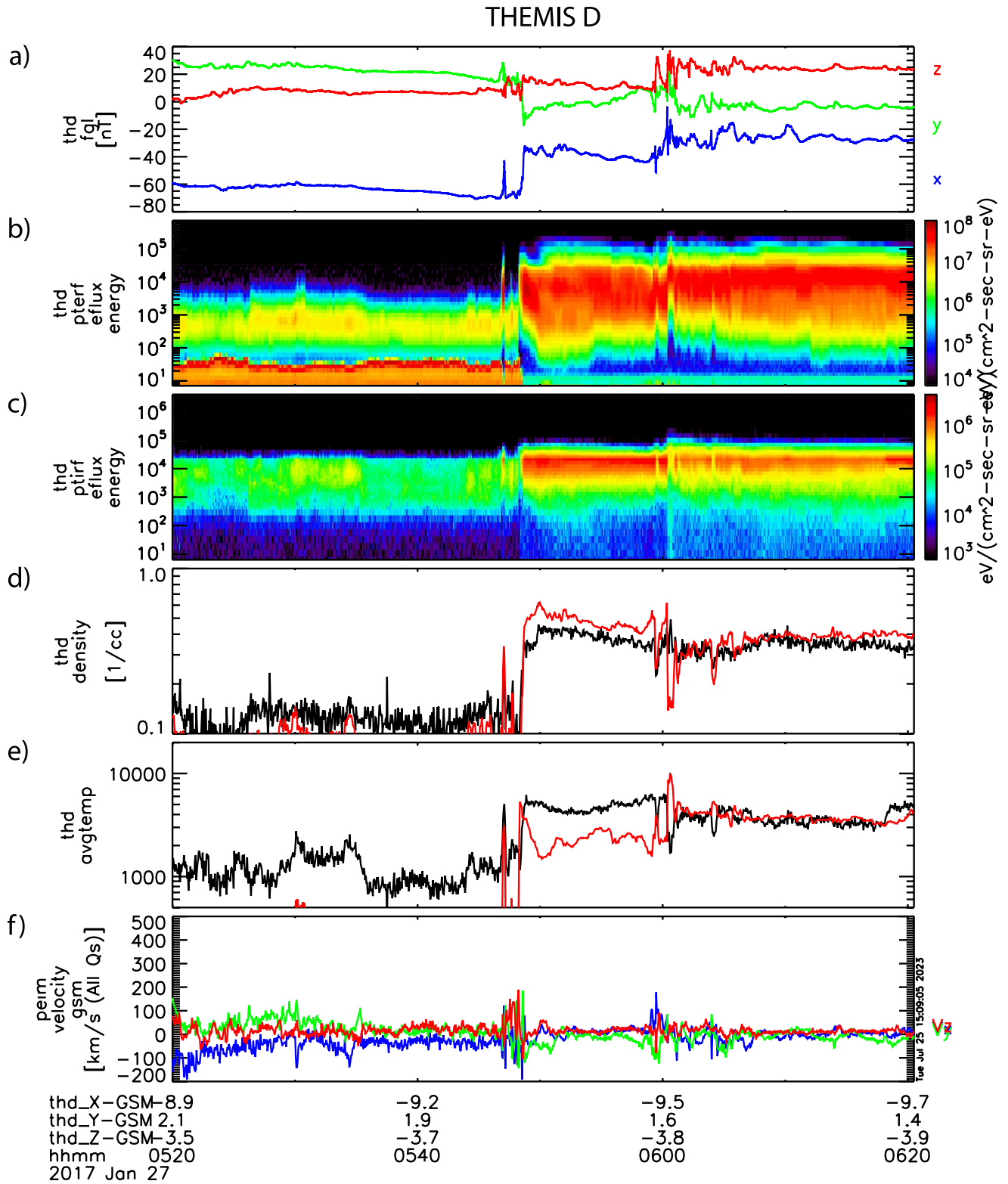


Figure 2. THEMIS D overview from 05:20 to 06:20 UT 27 January 2017. Panel (a) shows the three components of the magnetic field in GSM coordinates. Panels (b and c) are omnidirectional energy flux spectra of the differential energy flux of electrons and ions, respectively. Panels (d and e) show the ion density and ion (black) and electron (red) temperatures, respectively, and panel (f) shows the three components of the ion flow in GSM coordinates.

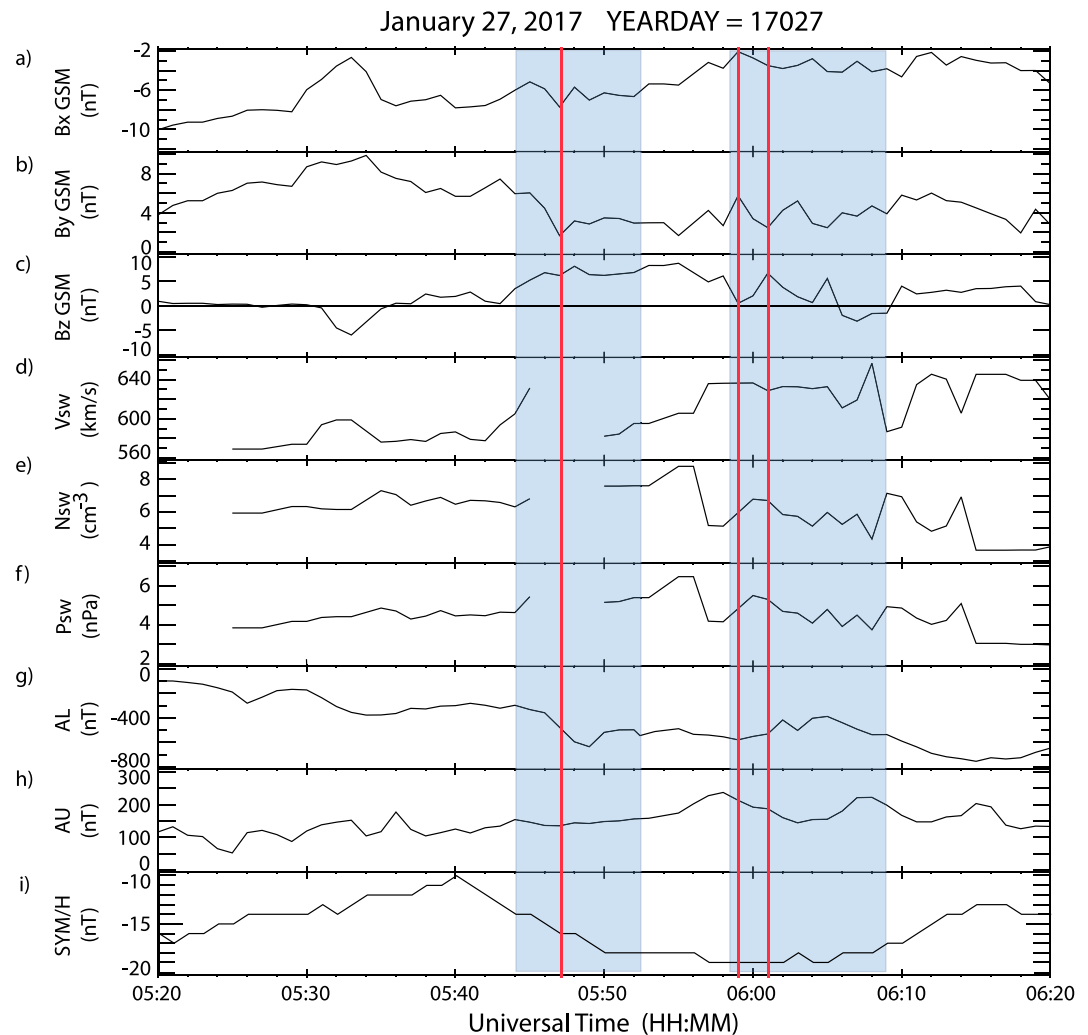


Figure 3. Time-shifted OMNI IMF and solar wind data (panels a–f) and the AL, AU, and SYM/H magnetic activity indices (panels g–i) from 05:20 to 06:20 UT 27 January 2017. The times of the DFBs observed by THEMIS D and E are indicated by vertical red lines, and the two shaded intervals show time intervals with nearly simultaneous GMDs observed by five ground magnetometers located along the west coast of Hudson Bay.

the first shaded interval and beyond it until 05:58 UT and dropped rapidly to +1 nT at 05:59 UT, the time of the second DFB at THEMIS D. It oscillated between +1 and +6 nT until 06:05 UT, dropped to –3 nT near 06:06 UT, and became positive again at 06:10 UT.

The solar wind velocity (V_{sw} , panel d) exceeded 565 km/s throughout the period shown. It rose to 630 km/s between 05:42 and 05:45 UT, 1 min after the start of the first shaded interval and just before a data gap. Data resumed at 05:50 UT, at which time V_{sw} was at 580 km/s. During the second shaded interval V_{sw} was again near 640 km/s. Before and during the two shaded intervals the solar wind proton number density (N_{sw} , panel e) varied between 4 and 8 cm^{-3} and the solar wind dynamic pressure (P_{sw} , panel f) varied similarly between 4 and 8 nPa.

The AL index (panel g) declined gradually but not monotonically from –50 nT at 05:20 UT to \sim –340 nT by 05:37 UT, and remained near that level until 05:44. It then dropped more rapidly to a minimum value of –600 nT at 05:49 UT, during the time the first DFB was observed (05:47 UT). From 05:49 UT to 05:50 UT it rose slightly to –500 nT. AL remained near –500 nT from 05:50 UT to 06:01 UT, during the time the second DFB was observed (05:59 and 06:01). From 06:01 it rose slightly to peaks near –400 nT at 06:02 and 06:04–05 UT before falling gradually from 06:05 to 06:15 to a value of –700 nT. The AL index appeared to respond to other activity, not the DFBs observed by THEMIS D and E. The AU index (panel h) ranged between 50 and 250 nT during the

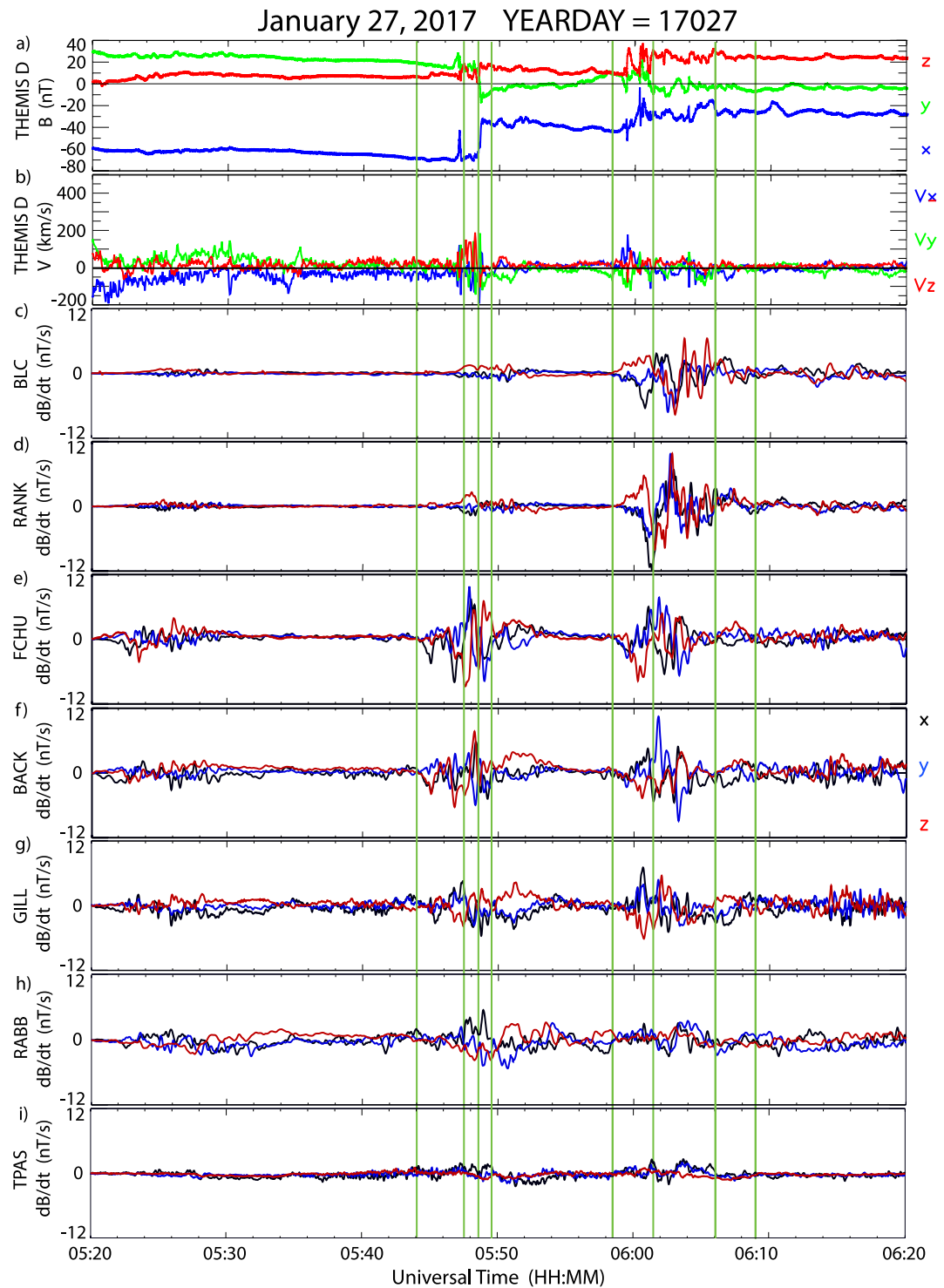


Figure 4. Composite plot showing simultaneous observations of the magnetic field and bulk velocity observed by THEMIS-D and the magnetic field observed by seven ground-based magnetometers, in order of decreasing latitude, from 05:20 to 06:20 UT 27 January 2017. Panels (a and b) show the GSM vector components of the magnetic field and bulk velocity observed by THEMIS-D. Panels (c–i) show three components of the time derivative of the magnetic field from BLC, RANK, FCHU, BACK, GILL, RABB, and TPAS, respectively, in local geomagnetic coordinates. The vertical green lines correspond to the times of SECS maps and composite all-sky images shown in Figures 6 and 7.

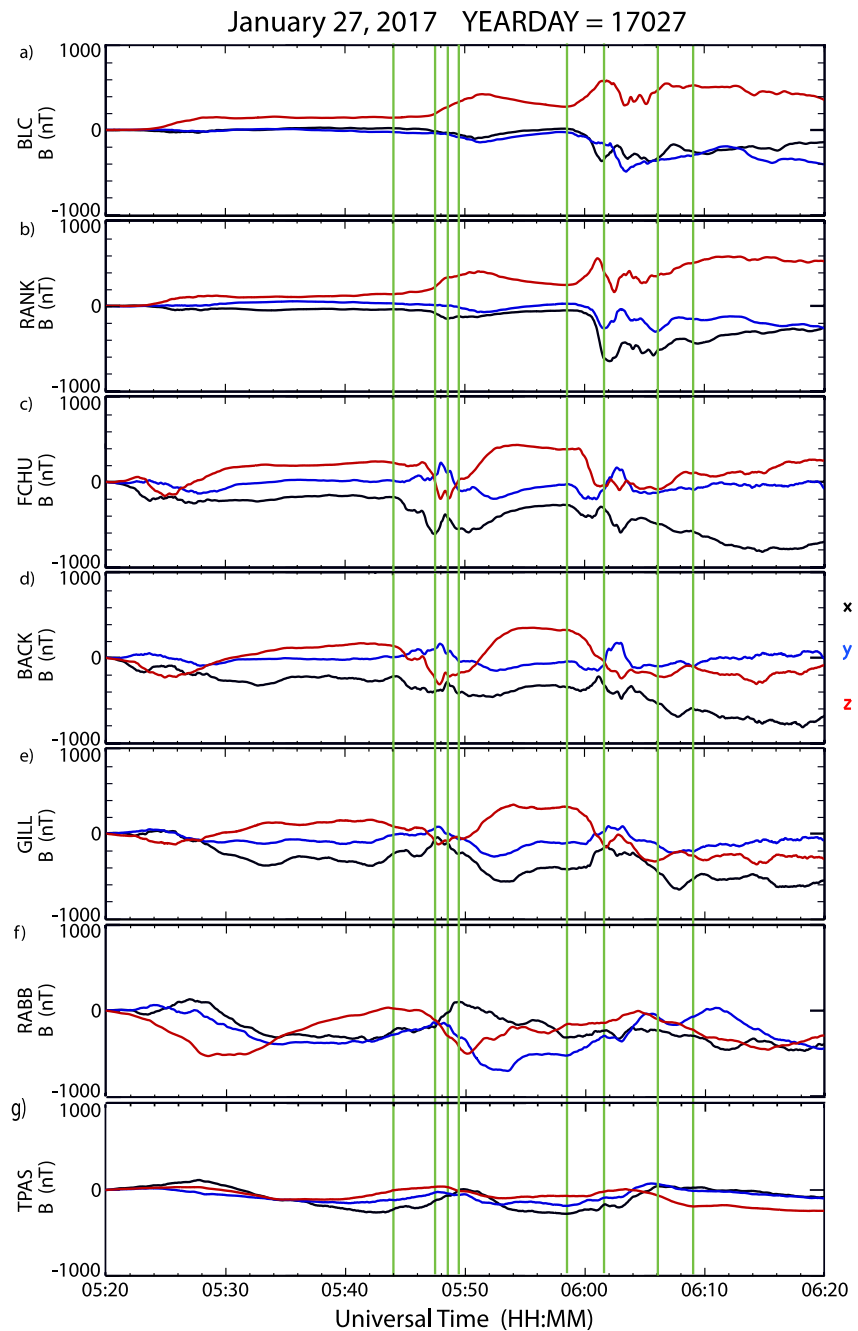


Figure 5. Composite plot showing the magnetic field observed by seven ground-based magnetometers, in order of decreasing latitude, from 05:20 to 06:20 UT 27 January 2017. Panels (a–g) show three components of the magnetic field from BLC, RANK, FCHU, BACK, GILL, RABB, and TPAS respectively, in local geomagnetic coordinates. The vertical green lines correspond to the times of SECS maps and composite all-sky images shown in Figures 6 and 7.

period shown, with values near 150 nT during both intervals. The SYM/H index (panel i) varied only slightly throughout the period shown, from -10 to -19 nT, indicating little or no geomagnetic storm activity. It dropped slightly between 05:40 and 05:50 UT (before and during the first DFB), and remained steady from 05:56 to 06:02 UT (during the second DFB).

The Newell and Gjerloev (2011), Forsyth et al. (2015), and Ohtani and Gjerloev (2020) substorm lists (each accessed on the SuperMAG web site at <https://supermag.jhuapl.edu/substorms/>) all included substorm onsets

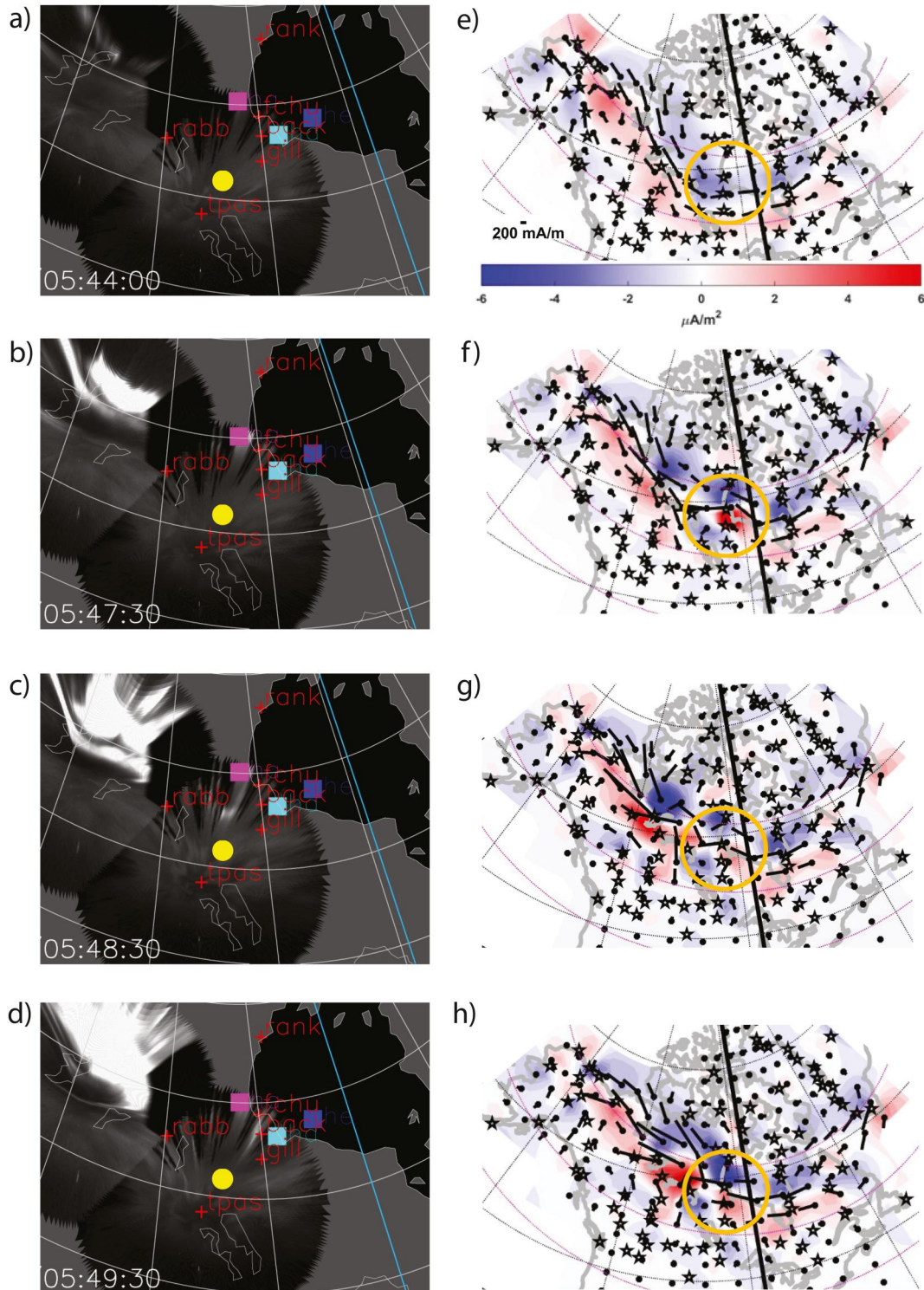


Figure 6. Simultaneous auroral images and SECS maps at times before and during the first DFB-GMD event shown in Figure 4. Panels (a–d) show composite all-sky auroral images at 05:44:00, 05:47:30, 05:48:30, and 05:49:30 UT, respectively, on 27 January 2017. The pink, aqua, and blue squares denote the footprints of THEMIS-A, -D, and -E, respectively. The locations of RANK, FCHU, BACK, and GILL near the western edge of Hudson Bay are shown by red crosses. The yellow dot shows the magnetic footprint of GOES 14. Panels (e–h) are maps at these same times of the equivalent ionospheric currents (black arrows) and vertical current intensities (upward in red, downward in blue) across northern North America and Greenland produced using the Spherical Elementary Current Systems method. The stars inside the yellow circle in each SECS image correspond to the locations of the magnetometer stations. The scale for the ionospheric currents and the color bar for the vertical currents are shown at the bottom of panel (e).

during this interval. All three lists included a substorm onset near 05:22 UT, but onsets at 05:44 UT and 06:04 UT were included only in the Newell and Gjerloev (2011) list, and an onset at 05:02 UT was included only in the Forsyth et al. (2015) list. The Newell and Gjerloev list identified the large negative jump in B_z at RANK as the location of the 06:04 UT substorm onset, which occurred shortly after a GMD appeared at THEMIS E, but no substorm ensued.

The combination of high V_{sw} , -10 to -20 nT SYM/H, and moderate auroral activity (AL and AU) including substorm activations is characteristic of a High Intensity Long Duration Continuous AE Activity (HILDCAA) interval, as described by Tsurutani and Gonzalez (1987). Tsurutani et al. (1995) noted that similar extended HILDCAA intervals observed during the declining phase of the sunspot cycle were characterized by continuous auroral substorms stimulated by large-amplitude Alfvén waves within the high-speed streams.

Figure 4 shows simultaneous observations from THEMIS-D and seven ground-based magnetometers along or somewhat west of the west coast of Hudson Bay, in order of decreasing latitude, from 05:20 to 06:20 UT 27 January 2017. Panels a and b show the GSM vector components of the magnetic field and bulk velocity observed by THEMIS-D (repeated from Figure 2). DFBs were identified at 05:46:58, 05:48:20, and 05:59:23 UT. Panels c, d, e, f, g, h, and i show three components of the time derivative of the magnetic field from BLC, RANK, FCHU, BACK, GILL, RABB, and TPAS, respectively, in local geomagnetic coordinates. The derivative amplitude of the first large GMD, observed between 05:44 and 05:53 UT, was largest at FCHU at 05:48 UT in the B_y component (9.38 nT/s) and B_z component (-9.11 nT/s), successively weaker to the south at BACK and GILL, and much weaker to the north at BLC and RANK. The derivative amplitude of the second large GMD, observed between 5:58 and 06:09 UT, was largest at RANK at 06:01 UT in the B_x component (-12.08 nT/s) and at 06:03 UT in the B_y component (9.65 nT/s), but also reached peak values above 6 nT/s at each of FCHU, BACK, AND GILL. the three other stations. The observations from RABB and TPAS will be discussed in Section 3.2 below, and the relative timing of the DFBs and GMDs will be discussed in Section 4.

Figure 5 shows the magnetic field from the seven stations shown in Figure 4, over the same time interval from 05:20 to 06:20 UT. The zero level of each component trace has been set to that component's value at 05:20 UT. The polarity of the component variations can help to reveal the relative locations of the ionospheric currents that drive these perturbations. A negative ΔB_x value indicates a westward current above a given station, and the polarity of the ΔB_z component can be used to infer the location of the westward current relative to the observing station, $\Delta B_z > 0$ for a westward current south of the station, and $\Delta B_z < 0$ for a westward current north of the station.

Before the first GMD (from 05:30 to 05:44 UT) the ΔB_x values were negative and ΔB_z values were positive at FCHU, BACK, and GILL, consistent with a westward electrojet south of these stations. During the first GMD (05:44–05:53 UT) rapid perturbations were evident in all three components at the three lower latitude stations (FCHU, BACK, and GILL), and weaker and more gradual changes appeared at BLC and RANK, associated with much weaker GMDs at these stations. A large 220 nT negative ΔB_x perturbation appeared at FCHU between 05:46 and 05:47:30 UT, immediately before the time of the first DFB and during the rise in amplitude of the GMD, and a much weaker ΔB_x perturbation (<50 nT) appeared at BACK. This allows us to infer the presence of a short-lived overhead westward electrojet (WEJ) that was closer to FCHU than to BACK, consistent with its larger GMD amplitude as shown in Figure 4. Between 05:44 and 05:48 UT, immediately before the DFB, the B_z traces at FCHU, BACK, and GILL all became more negative by 400, 460, and 180 nT, respectively, but increased gradually after the DFB until 05:53 UT by 600, 500, and 380 nT, suggesting that the WEJ widened and intensified until then, when it became stationary.

During the second GMD (05:58:30–06:09 UT) rapid perturbations were evident at all five stations. A -270 nT minimum in ΔB_x appeared at BLC at 06:01 UT, was much larger (-580 nT) at RANK at 06:02 UT, and was successively weaker at FCHU (-280), BACK (-220), and GILL (-100 nT) near 06:03 UT, suggesting a highly localized westward current after 06:01 UT. The growth of a subsequent broad westward current over FCHU, BACK, and GILL can be seen in the gradual drop in ΔB_x between 06:03 and 06:09 UT at these stations.

The following paragraphs will describe auroral images and calculations of ionospheric and up/down currents using the SECS method that are consistent with these GMDs and magnetic perturbations. Figure 6 shows composite all-sky images and SECS maps at 05:44, 05:47:30, 05:48:30, and 05:49:30 27 UT January 2017, before and during the first DFB-GMD pair shown in Figure 4. Figures 6a–6d are images from Movie S1 (included in Supporting Information S1) prepared by the THEMIS project showing all sky camera mosaics from Fort Smith

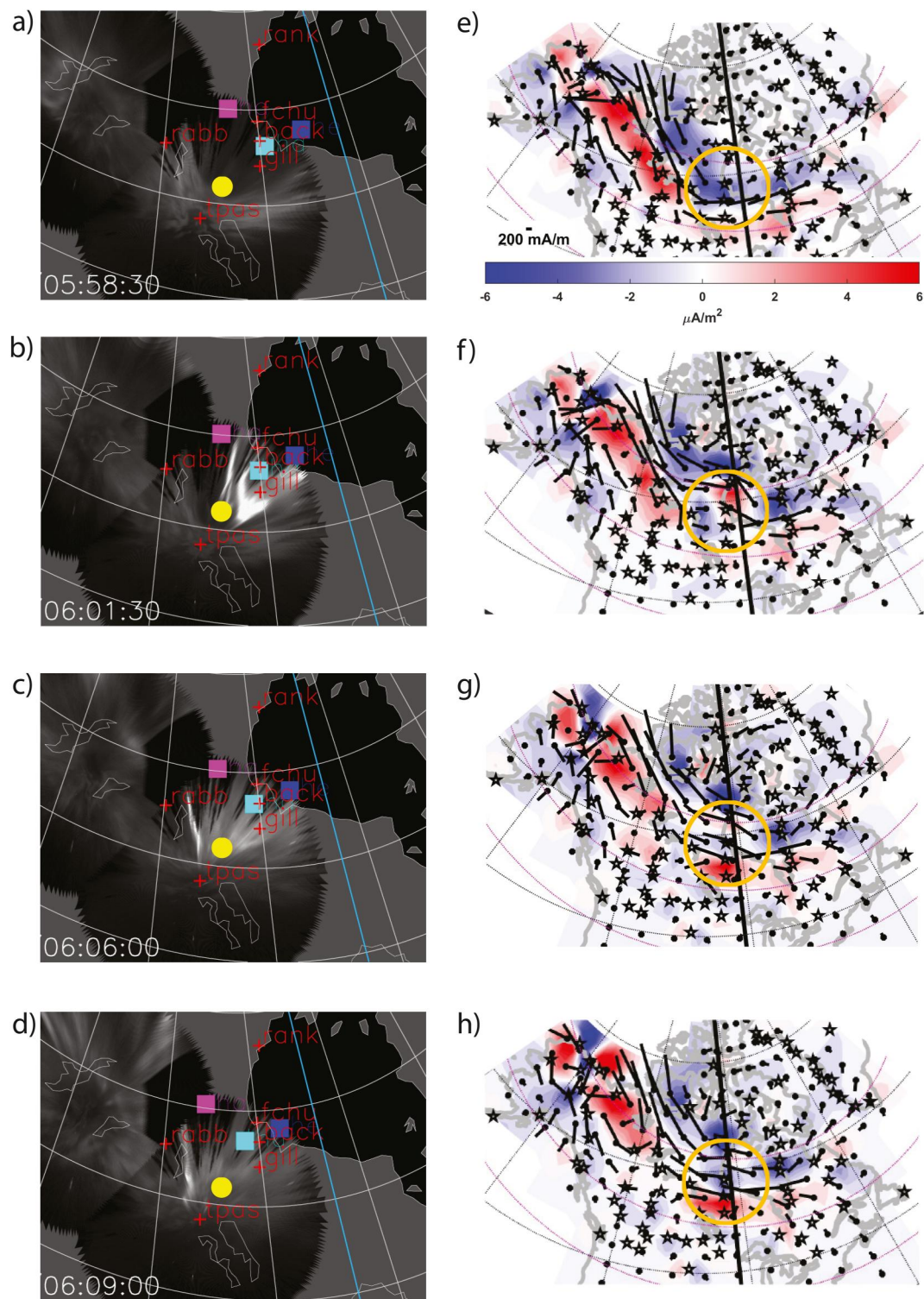


Figure 7. Composite all-sky auroral images and SECS maps as in Figure 6, but at 05:58:30, 06:01:30, 06:06:00, and 06:09:00 UT on 27 January 2017.

and The Pas projected geographically onto a map of central and eastern Canada. The fields of view of the cameras are evident from the two circles. Auroral images from Fort Smith and The Pas extended over FCHU, BACK, and GILL but did not reach to RANK or BLC, and much of the field of view of the Fort Smith imager north of RABB was blocked by a mask because of light contamination, so there is no data in that region.

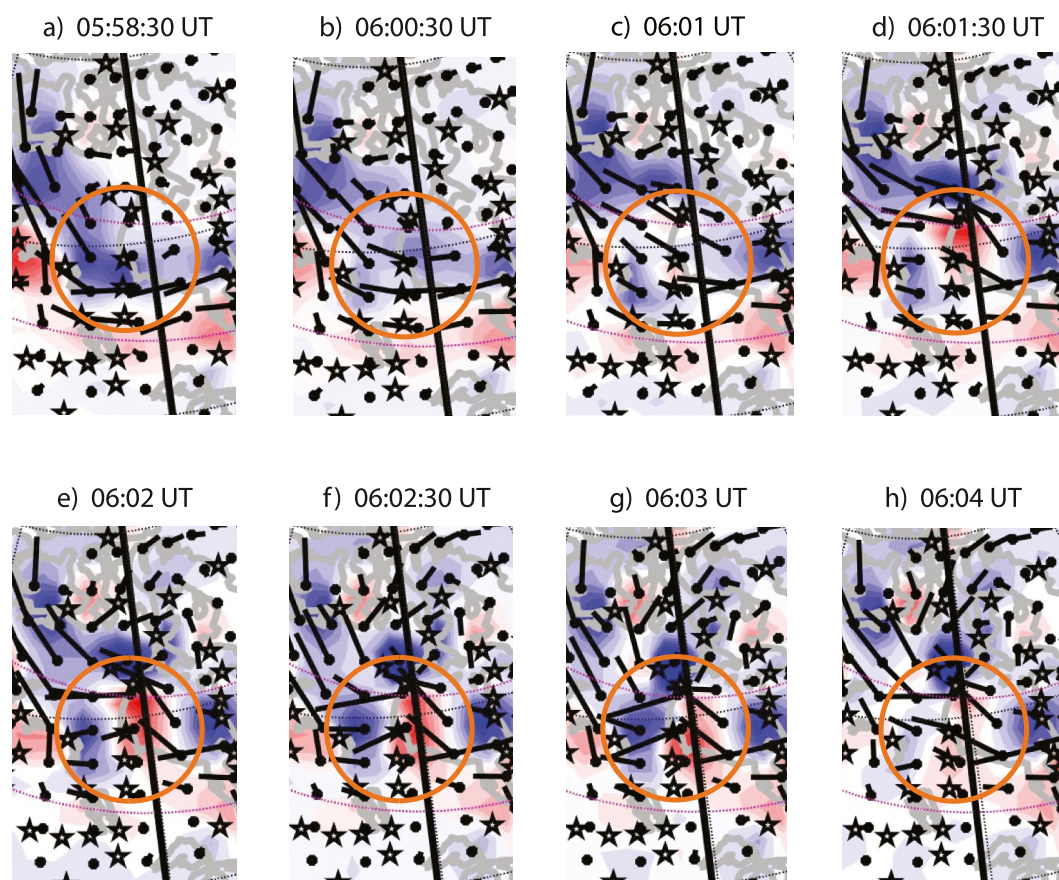


Figure 8. Zoomed-in SECS maps as in Figures 6 and 7, but at 05:58:30, 06:00:30, 06:01, 06:01:30, 06:02, 06:02:30, 06:03, and 06:04 UT on 27 January 2017.

Parallels and meridians in magnetic coordinates are shown in white, and the light blue meridian denotes local magnetic midnight. The pink, aqua, and blue squares denote the footpoints of THEMIS-A, -D, and -E, respectively, determined using the Tsyanenko-2001 magnetic field model (Tsyanenko, 2002a, 2002b) for field line tracing. The locations of RANK, FCHU, BACK, GILL, RABB, and TPAS are shown by red crosses. The yellow dot shows the magnetic footpoint of GOES 14. The footpoints of the three THEMIS spacecraft were nearly stationary in Figures 6a–6c, with THEMIS A slightly northwest of FCHU, THEMIS D just east of BACK, and THEMIS E slightly farther to the northeast, over southwestern Hudson Bay.

Only very weak auroras appeared anywhere in the field of view of the imagers at 05:44 UT (Figure 6a), before the start of the first GMD shown in Figure 4. At 05:47:30 UT (Figure 6b), near the time of the largest derivative of the GMD in the FCHU data, the tip of an auroral streamer appeared over FCHU, partly obscured by the pink square. By 05:48 UT the equatorward edge of the streamer had extended to the west of BACK (not shown) and at 05:48:30 UT (Figure 6c) its equatorward edge had reached a point southwest of BACK. The streamer then faded rapidly, and was no longer visible in the 05:49 UT image. A second streamer appeared to the east of the first one above and to the west of BACK at 05:49:30 UT, but it disappeared by 05:50 UT (not shown). Bright east-west arcs appeared far to the northwest of FCHU at 05:47:30 and more extended and complex auroral arcs filled much of the region to the northwest at 05:48:30 UT, but these were not connected to the activity immediately west of Hudson Bay. The weak auroral glow that appeared over and to the south of GILL at 5:44 was unchanged by 05:48:30.

Figures 6e–6h are SECS maps of the equivalent ionospheric currents (black arrows) and vertical current intensities (upward in red, downward in blue) across northern North America and western Greenland at the same times as Figures 6a–6d. The stars show the locations of magnetometers providing data on this day, and the dots show the grid points at which the horizontal currents were calculated. The yellow circle in each of these maps

outlines the region of interest; the four stars it encloses correspond to the locations of the magnetometer stations near the western edge of Hudson Bay.

Figure 6e shows that at 05:44 UT a narrow westward electrojet passed through BACK and GILL, and a weak downward current region (blue) extended westward of BACK and FCHU. An intense and highly localized upward current region (red) suddenly appeared in the SECS map at 05:47 UT (not shown) and was most intense at 05:47:30 UT (Figure 6f) between FCHU and BACK in association with a somewhat more extended region of downward current between RANK and FCHU and a latitudinally localized WEJ with a slight counter-clockwise vortical arc immediately north of FCHU. This current pair had not moved but was somewhat weaker by 05:48 UT (not shown) but by 05:48:30 (Figure 6g), the region of upward current had moved southward above and east of GILL and was much weaker, and the region of downward current had moved northward. By 05:49:30 UT the downward current region intensified and moved rapidly southward to just north of FCHU and the upward current region moved westward over BACK. This localized upward current remained near BACK and GILL until it faded out at 05:54:30 (not shown), consistent with the presence of a weaker GMD at FCHU, BACK, and GILL during this time (Figure 4).

Figure 7 shows composite all-sky images and SECS maps at 05:58:30, 06:01:30, 06:06, and 06:09 UT on 27 January 2017, before, during and after the second DFB-GMD pair shown in Figure 4. The footpoints of the three THEMIS spacecraft resumed their slow westward motion during this time interval, with THEMIS A slightly northwest of FCHU, THEMIS D above and later slightly west of BACK, and THEMIS E approaching the southwestern coast of Hudson Bay. Weak auroras appeared at some distance to the south and west of Hudson Bay at 05:58:30 UT (Figure 7a), before the start of the second GMD shown in Figure 4, but there was very little auroral intensity above any of the magnetometer stations at the west end of Hudson Bay. Figure 7e shows that at 05:58:30 UT the westward electrojet (WEJ) continued across Hudson Bay through BACK before turning to the northwest and both broadening and intensifying as it extended toward Alaska. This WEJ was bounded by an extended region of strong downward current (blue) to the northeast and an extended region of strong upward current (red) to the southwest. The southeastern end of the strong downward current (blue) ended between FCHU and BACK, but there were no upward currents near the four magnetometer sites.

At 06:01:30 UT (Figure 7b), shortly after the time of the largest derivative in the BACK data, a bright, narrow auroral streamer appeared to the west of FCHU, and a double-pronged streamer was visible nearly overhead of BACK and to the northeast and immediately southwest of GILL. Figures 7f and 8a–8d show that a moderately strong localized upward current (red) appeared suddenly at 06:01:30 UT between RANK and FCHU, and the westward electrojet veered to the northwest in a partial counterclockwise vortex and resumed its westward orientation north of RANK in association with a downward current. This structure in the currents, similar to that noted in Figure 6f, is most likely consistent with the streamer wedge current system shown in the schematic diagram of auroral streamers and associated currents in Figure 1 of Weygand et al. (2022). Figures 8d–8h show that the region of upward current north of FCHU subsequently moved equatorward, reaching a location between BACK and GILL by 06:03 UT and then fading from view by 06:04 UT. This upward current region intensified at 06:05 UT (not shown), became very strong at 06:06 UT (Figure 7g) and diminished very gradually until 06:20 UT (not shown), but remained separated from the downward current region north of FCHU. Figure 7c shows that by 06:06 UT the streamer had expanded and weakened as it moved to the southwest, and another streamer appeared to the west between it and RABB. The activity in this region will be addressed further in the next section. By 06:09 UT (Figure 7d), several minutes after the end of the intense GMD, only weak auroral activity remained over and southwest of FCHU, BACK, and GILL. Figure 7h shows that at 6:09 UT the region of upward current between BACK and GILL extended farther west but remained strong between these two stations and the region of downward current remained over RANK, but was separated by a relatively wide and consistently westward electrojet from the region of upward current.

3.2. GOES 14 and RABB Observations on 27 January 2017

The footpoint of GOES 14 was located ~590 km southwest of FCHU and west of the streamers overhead of the magnetometer stations. In this section we describe the GOES 14 observations as well as magnetometer observations from RABB and TPAS, and compare them to the ASI movie images and SECS maps.

Figure 9 shows stacked plots of the differential electron flux (panel a) and ion flux (panel b) recorded by Telescope 1, the Hp component of the magnetic field observed by GOES 14 (panel c), and the SMU (red) and

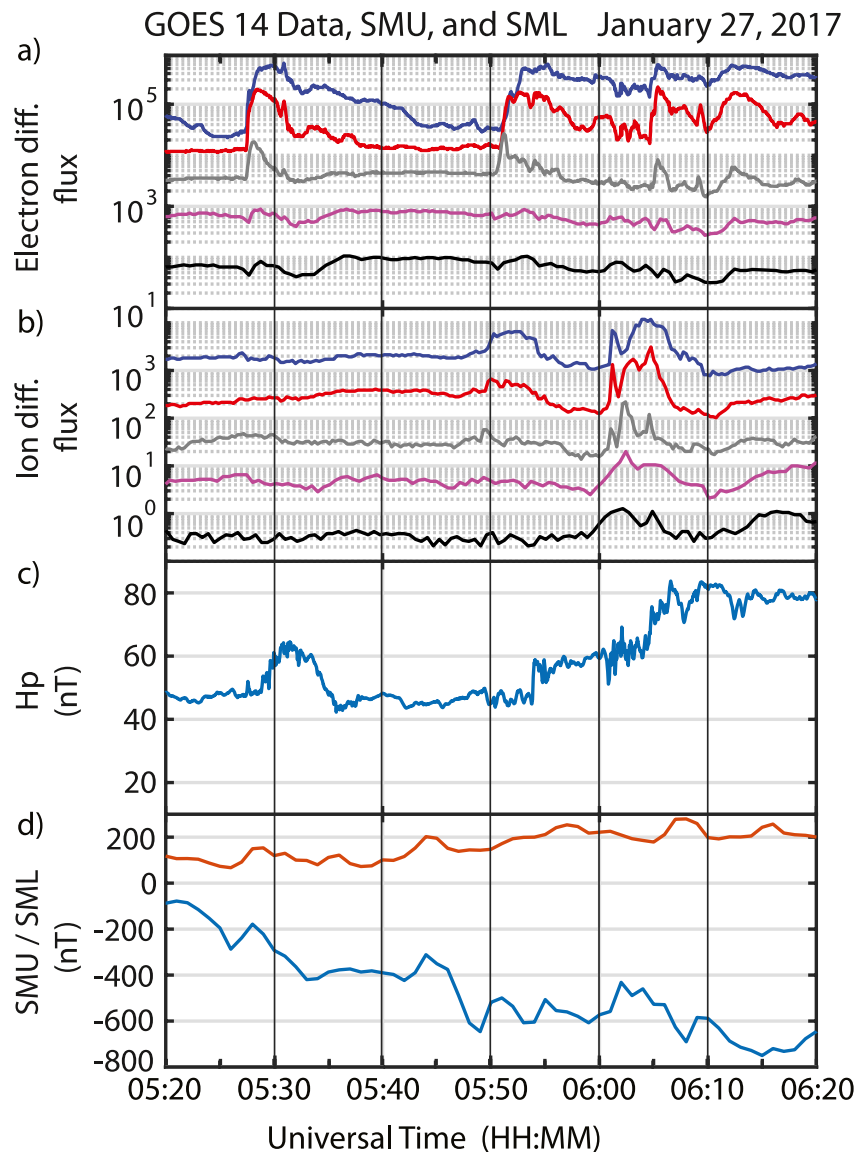


Figure 9. Stacked plots of GOES 14 energetic particle and magnetic field data and magnetic activity index data from 05:20 to 06:20 UT on 27 January 2017. Panel a shows the differential directional electron number flux in five energy ranges (blue 30–50 keV, red 50–100 keV, gray 100–200 keV, pink 200–350 keV, and black 350–600 keV), and panel b shows ion flux in five energy ranges (blue 80–110 keV, red 110–170 keV, gray 170–250 keV, pink 250–350 keV, and black 350–800 keV), respectively, both in units of $\text{cm}^{-2} \text{s}^{-1} \text{sr}^{-1} \text{keV}^{-1}$. Panel c shows the Hp component (approximately northward) of the magnetic field from the outboard magnetometer. Panel d shows the SMU (red) and SML (blue) auroral activity indices.

SML (blue) indices (panel d), from 05:20 to 06:20 UT. The fluxes shown in Figures 9a and 9b were observed by Telescope 9 of GOES-14 MAGED and MAGPD. Because GOES-14 was flying inverted during this period, Telescope 9 of each instrument was looking southward in the anti-field-aligned direction, thus observing the most nearly field-aligned fluxes (Jaynes et al., 2013). The pitch angles varied with the natural variations in the geomagnetic field orientation observed by the GOES-14 magnetometer (Rodríguez, 2014). Between 05:20 and 06:20 UT, the Telescope 9 central pitch angle (not shown) was on average 12.4° with a range of $5.7\text{--}23.5^\circ$. The bounce loss cone in GEO ($\sim 2.5^\circ$) is much smaller than the MAGED and MAGPD telescope FOV (20 deg FWHM). Owing to the satellite orientation, the FOV size and the small central pitch angles, the Telescope 9 FOV fluxes included both loss-cone and near-loss-cone fluxes during most of this period, as in the case studied by Jaynes et al. (2013).

Electron fluxes (Figure 9a) showed a sharp energy-dispersed increase at 05:51 and a smaller rapid, dispersionless increase at 06:05, in each case ~ 3 min after the maxima in the GMDs shown in Figure 4, and flux peaks at $\sim 05:54$ and $\sim 06:06$ UT. Smaller increases in ion flux (Figure 9b) appeared slightly earlier, at 05:49 and 06:01 UT (also energy-dispersed and dispersionless, respectively), and increases in H_p , indicating dipolarizations occurred near 05:54 and 06:04 UT (Figure 9c). These dispersion characteristics suggest that GOES-14 was east of the site of the first injection and closer to the site of the second injection. The large downward trend in SML from 05:20 to 06:20 UT (Figure 9d) is indicative of increasing substorm activity.

Movie S1 shows that only faint, featureless auroras appeared within ~ 400 km of the west Hudson Bay coast stations between 05:40 and 05:46 UT (shown for example in Figure 6a), and after 05:42 UT only faint auroral activity was observed in the field of view of either the Fort Smith or The Pas cameras except near the northern end of the Fort Smith image. This aurora brightened and expanded toward the southeast beginning near 05:45 UT. At 05:50 UT a faint northwest to southeast streamer first appeared south of RABB, and at 05:50:30 it was joined by a second parallel streamer to the east. By 05:51 UT, as these streamers intensified and moved farther southeast, there was some evidence despite the large masked region north of RABB that they were connected to the large region of intense aurora northwest of the masked region. These streamers strengthened and moved slightly southeast during 05:52 and 05:53 UT, reached TPAS at 05:55 UT, and then stalled and began to fade. Another weaker streamer appeared to the southwest of RABB at 05:52 UT, and similarly stalled and began to fade after 05:55 UT.

Beginning at 05:50 UT a latitudinally broad region of modest-amplitude east-west aurora that stretched from the eastern edge of the TPAS ASI's field of view westward to near the GOES 14 footpoint began to gradually intensify. It became slightly stronger by 05:53 UT, reached overhead of the GOES 14 footpoint from 05:55 to 05:56 UT, and then moved slightly equatorward and weakened by 06:01 UT. The increase in GOES 14 electron flux from 05:50 to 05:53 and its subsequent modest decrease to 06:01 UT are consistent with these images. There was however no simultaneous auroral activity above FCHU, BACK, or GILL between 05:50 and 06:00 UT. The lack of simultaneity between the electron flux peak observed by GOES 14 and the DFBs and GMDs observed by magnetometers along the west coast of Hudson Bay is consistent with the ~ 450 km longitudinal separation between these locations and the highly localized nature of the GMDs and their associated field-aligned currents and auroral signatures during this event.

Movie S1 shows that during the second DFB-GMD event at 06:03 UT a new streamer appeared to the west of those shown in Figure 7b at 06:01:30 UT. It was the first of a progression of streamers, each located west of the previous one; each of the existing streamers irregularly faded in turn. This process continued until 06:07 UT, at which time the most westward streamer had reached just to the east of RABB. This streamer remained stationary until 06:09 UT and began to fade at 06:10, at which time another streamer appeared slightly farther west.

Movie S1 also shows that the equatorward edge of the complex streamer that moved southwest from GILL (Figure 7b) was east of but close to the GOES 14 footpoint at 06:02 UT, overhead of it but weaker at 06:03 and 06:04 UT, and had retreated northward by 06:04:30 UT. At 06:05 UT a second region of aurora emerged west of BACK and GILL and moved to the southwest, and by 06:06 UT it had expanded to the GOES 14 footpoint (Figure 7c). It was strongest near the GOES 14 footpoint between 06:06 and 06:06:30, but by 06:07 UT it began to slowly fade and move northward by 06:07 UT, and by 06:10 it had faded significantly in the region above and slightly to the north of the GOES 14 footpoint. During this second DFB-GMD interval auroral emissions at GOES 14 and above and to the west of FCHU, BACK, and GILL were evidently part of the same system.

Figures 4f–4h show that an extended ≤ 2 nT/s GMD interval began at BACK and GILL at 05:20 UT and 2 min later at RABB, located 562 km west of BACK, and persisted at a low level until 05:44 UT. The peaks of the first large GMD appeared at BACK between 05:46:30 and 05:47:30 UT, and ~ 2 min later at RABB (05:47:30–05:49 UT). The latter coincided with the appearance of a strong up/down current pair in SECS data (Figures 6g and 6h) over RABB between 05:48 and 05:50 UT that was unrelated to the simultaneous current pair and streamer above FCHU. Figure 4i shows only very weak derivative activity at TPAS, located 202 km southwest of FCHU. Only its larger amplitude at 06:04 UT correlated with the increased electron flux observed at GOES 14.

After 05:50 UT a lower amplitude GMD (2–4 nT/s) appeared at both GILL and RABB; it persisted slightly longer at RABB, and 2 nT/s activity appeared only at RABB between 05:56:30 and 05:58:30 UT. SECS maps showed that RABB remained between a pair of strong up and down currents between 05:50 and 05:58:30 UT, when they

began to weaken. The second large GMD did not appear at all in the RABB data. Instead, a 4 nT/s GMD appeared beginning at 06:02 UT. This GMD coincided with the slight intensification at 06:02 UT (not shown) of an extended and relatively weak up/down current pair west and east of RABB, respectively that appeared at 06:01:30 UT (Figure 7b) and was separate from the current pair north of FCHU.

The ΔB traces from RABB (Figure 5f) showed different and slightly more rapid perturbations before the first GMD at 05:47 UT, between the first and second GMDs, and again after the second GMD. Rapid changes occurred during the first GMD, but not during the second GMD until after its conclusion. The ΔB traces from TPAS (Figure 5g) were very weak, and again correlated with the increased electron flux observed at GOES 14 only between 06:04 and 06:06 UT.

Although a northwestward electrojet appeared in SECS maps above and to the northwest of RABB with varying but often strong intensity during and between both GMD intervals, we have noted that only when upward and downward current regions were in close proximity above RABB was any significant GMD observed there, and the GMD amplitudes were not as large as those observed by stations in the Churchill line. Only very weak auroras were evident in Movie S1 below or south of RABB during either GMD event, but as noted above no data were available in the large masked region north of RABB.

3.3. 7 January 2017

Figure 10 shows a summary plot of THEMIS E observations between 04:40 and 06:00 UT on 7 January 2017 in the same format as in Figure 2. Evidently, the probe was deep in the plasma sheet near the magnetic equator. The plasma sheet was abundant with energetic electrons: significant fluxes of electrons were detected at energies of 100–500 keV. During the interval of interest, THEMIS E detected a set of quasi-recurrent magnetic field dipolarizations (increases in B_z) at 04:51:27, 05:09:20, 05:25:12, and 05:51:40 UT. The first three DFBs were observed at THEMIS D from 1 to 2 min later, at 04:53:31, 05:11:11, 05:26:58, and the fourth slightly earlier at 05:51:10 UT (not shown). The dipolarizations were preceded by intervals of magnetic field stretching, characterized by increases in B_x magnitude and decreases in B_z . Each dipolarization was associated with a decrease in density, which is characteristic of DFBs, an enhancement in the plasma bulk flow, and an energetic (up to 700 keV) electron injection. No significant energetic ion injections were detected. The electron temperature increased at each dipolarization and became comparable and even exceeded the ion temperature. It is also worth noting that the bulk flow enhancements exhibited vorticity: large-amplitude variations with sign changes were detected in all three velocity components. The evident flow vorticity might indicate that the bursty flows associated with the dipolarizations were detected at or close to their stoppage points (e.g., Birn et al., 2019; Panov et al., 2010, 2013).

No time-shifted OMNI data were available during this interval. Although IMF and solar wind data were available near the L1 point from ACE, DSCOVR, and WIND, their values showed moderate to large disagreements in all three magnetic field components, as well as in N_{sw} , P_{sw} , and V_{sw} . We show instead in Figure 11 time-corrected IMF and solar wind data from ARTEMIS P2 (THEMIS C), in orbit around the moon at $X_{GSM} = -16.70 R_E$, $Y_{GSM} = 52.33 R_E$, $Z_{GSM} = 1.26 R_E$, ~ 5 min downstream of Earth's bow shock and azimuthally at a similar distance from the Earth-Sun line as WIND. The vertical red lines in Figure 11 indicate the times DFBs were observed at THEMIS E and D, respectively, and the shaded region indicates a time interval surrounding the third DFB to be examined in greater detail in Figures 14 and 15.

Figures 11a and 11b show that the IMF B_x component varied in direction often during this 80 min interval, while IMF B_y varied with similar amplitude but was mostly negative. The first DFB occurred under fairly steady -2 nT B_z conditions, the second coincided with a rapid drop in B_z from ~ 0 to -3 nT, the third occurred immediately after a rise in B_z from -4 to $+1$ nT, and the fourth occurred under fairly steady -2 to -3 nT conditions. The earthward component of V_{sw} , the solar wind speed (Figure 11d), was near 700 km/s until $\sim 05:20$ UT, when it dropped briefly to 625 km/s, but then gradually increased to ~ 680 km near the end of the interval. V_{sw} was high before this interval as well: during all of the previous day (January 6) and up to the OMNI data gap near 04:30 UT on January 7, OMNI data (not shown) indicated that V_{sw} exceeded 650 km/s, indicating an extended interval of HILDCAA activity.

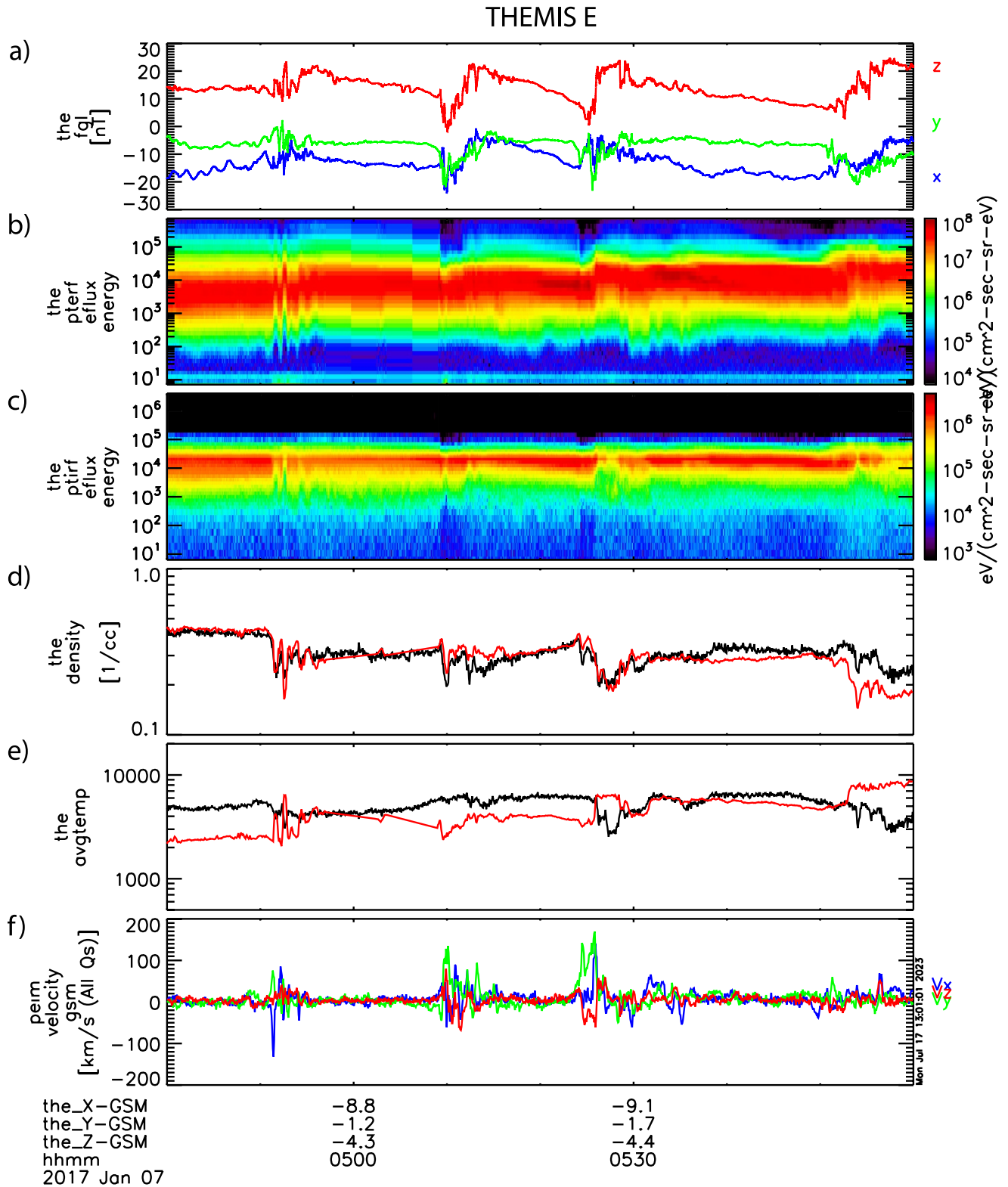


Figure 10. THEMIS E overview from 04:40 to 06:00 UT 7 January 2017, as in Figure 2.

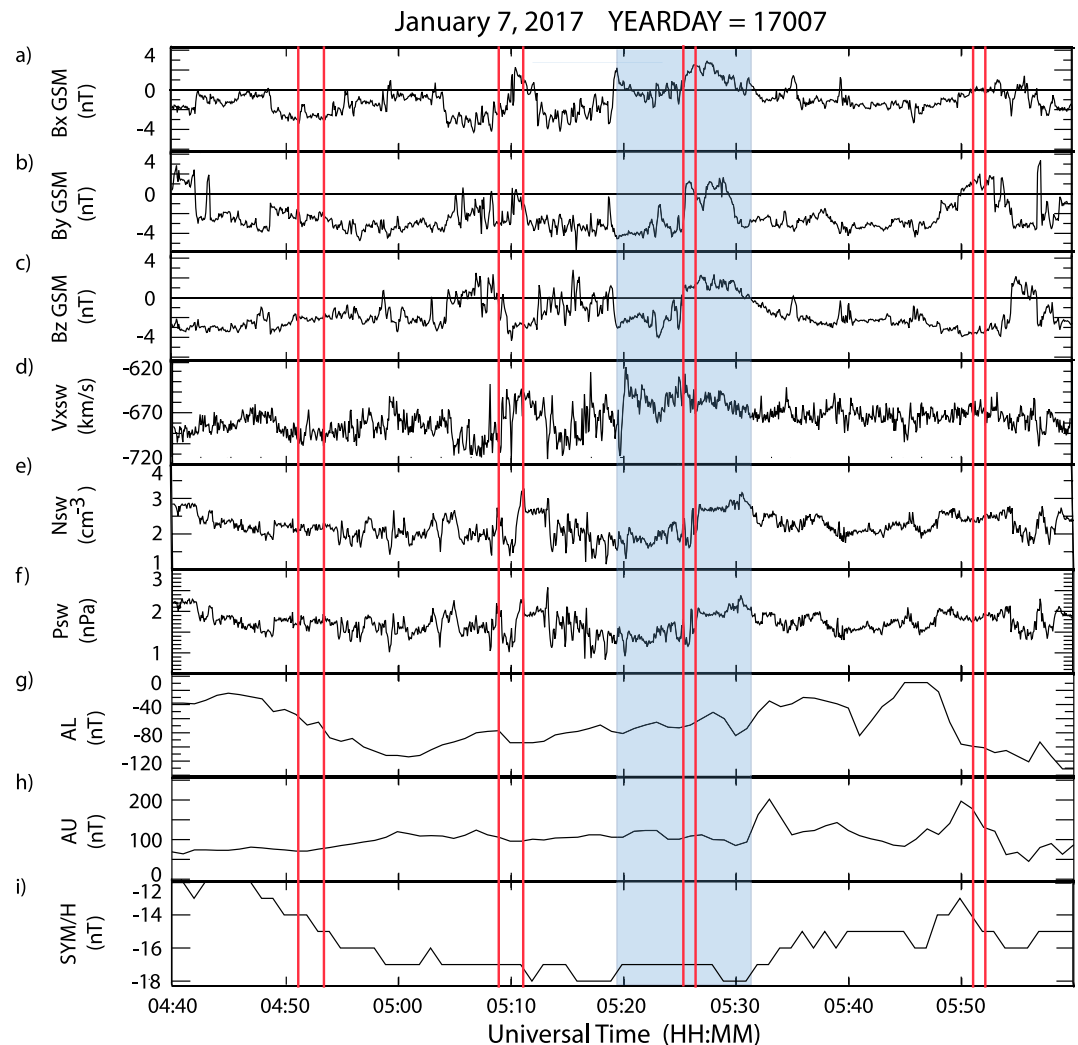


Figure 11. ARTEMIS P2 (THEMIS C) IMF and solar wind data time-shifted to the nose of the bow shock (panels a–f), and AL, AU, and SYM/H magnetic activity indices (panels g–i) from 04:40 to 06:00 UT 7 January 2017, as in Figure 3. The times of the DFBs observed by THEMIS D and E are indicated by vertical red lines, and the shaded interval shows a time interval with nearly simultaneous DFBs observed by THEMIS E and GMDs observed by ground stations near the east coast of Hudson Bay.

Figure 11e shows that the solar wind density N_{sw} was at or below 3 cm^{-3} throughout this interval. The solar wind dynamic pressure P_{sw} , shown in Figure 11f, remained below 3 nPa throughout this interval; its variations were very similar to those of N_{sw} .

The AL index (Figure 11g) declined gradually from -20 nT at 04:45 to -110 nT at 05:00 UT, during the time of the first DFB. It then rose gradually to -80 nT at 05:09 UT, then dropped to -100 nT at 05:10 UT, at the start of the second DFB. From 5:20 to 5:28 it rose unsteadily from -80 nT to -50 nT at 05:28 UT, during the time of the third DFB. It dropped rapidly from -10 at 05:47 UT to -100 nT at 05:50 UT, just before the fourth DFB, and dropped slowly from 05:50 UT to -120 nT at 05:57 UT. The first, third, and fourth DFBs coincided with small decreases in AL. The AU index (Figure 11h) rose during the time of the first DFB, fell during the second, was nearly constant at 100 nT during the third, and fell during the fourth.

The SYM/H index (Figure 11i) varied between -12 and -18 nT between 04:40 and 06:00 UT, again indicating little geomagnetic storm activity. It dropped slightly during the first DFB, remained steady during the second and third, and dropped again slightly during the fourth. The lack of any clear connection between B_z values or changes and DFB occurrences may mean either that the observed B_z values do not represent those impinging on Earth's

magnetosphere, or that under the high-speed solar wind conditions on this day the IMF Bz component's value did not play a major role in triggering the magnetotail reconnection that generated these DFBs.

Both the Newell and Gjerloev (2011) and Forsyth et al. (2015) substorm lists on SuperMAG included a substorm onset near 05:23 UT, and an onset at 04:48 UT was included only in the Forsyth et al. (2015) list. The Newell and Gjerloev list identified the negative jump in Bz at CDR as the location of the 05:23 UT onset and the Forsyth et al. list identified the more sustained negative jump in Bz at SALU as the location of the 05:21 UT onset. Neither time was listed as an onset in the Ohtani and Gjerloev list. Both of these onsets occurred slightly before GMDs appeared at THEMIS E, but no substorm ensued. This interval is again typical of HILDCAA events.

Figure 12 shows simultaneous observations from THEMIS E and five ground-based magnetometers near the east coast of Hudson Bay, in order of decreasing latitude, from 04:40 to 06:00 UT 7 January 2017, as in Figure 4. Panels a and b show the GSM vector components of the magnetic field and bulk velocity observed by THEMIS E (repeated from Figure 10). Panels c, d, e, and f show three components of the time derivative of the magnetic field from CDR, SALU, PUVR, INUK, and KJPK, respectively, in local geomagnetic coordinates. Amplitudes of the GMDs at times corresponding to all three DFBs exceeded 6 nT/s at SALU; the largest dB/dt value was 9.50 nT/s in the Bz component at 05:27 UT. GMDs coincident with the DFBs recorded at 04:51:27, 05:09:20, and 05:25:12 UT appeared at SALU and more weakly at PUVR and INUK, and the first and third coincided with moderate and strong GMDs at CDR.

Weaker and longer-lasting magnetic variations appeared at CDR beginning at 05:39 UT, at SALU and PUVR beginning at 05:48 UT, and at INUK at 05:52 UT. The variations at SALU, PUVR, and INUK might be related to the DFB at 05:51 UT, but the variations at CDR do not appear to be related to any of the perturbations observed by the two THEMIS spacecraft. The relative timing of the first three DFB—GMD pairs will be discussed in Section 4 below.

Figure 13 shows the magnetic field from the five stations shown in Figure 12, over the same time interval from 04:40 to 06:00 UT. The zero level of each component trace has been set to that component's value at 04:40 UT. The first three GMDs shown in Figure 13 clearly correspond to rapid perturbations in the magnetic field components, and the polarity of the component variations can help to reveal the relative locations of the ionospheric currents that drive these perturbations. In Figures 14 and 15 we will show that these traces provide information consistent with that provided by calculations of ionospheric and up/down currents using the SECS method. At this point we simply note that negative perturbations in Bz between 05:24 and 05:27 UT (associated with the third DFB) can be used to infer the presence of a nearly overhead westward electrojet that is closer to CDR than to SALU because of its larger amplitude, and that negative Bx perturbations in the red shaded region between 05:29 and 05:31 UT correspond to a separate westward electrojet that propagated equatorward from SALU to INUK as it weakened. Similarly, the polarity of the Bz component can be used to infer the location of the westward electrojets relative to the observing station, $\Delta B_z > 0$ for a westward current south of CDR, and $\Delta B_z < 0$ for a westward current north of SALU. It is evident that for both DFBs 1 and 3 the CDR and SALU ΔB_z polarities suggest that a westward current was located between these stations.

Figure 14 shows all-sky images and SECS maps at 05:19, 05:26:30, and 05:28 UT on 7 January 2017, before, during, and immediately after the third DFB-GMD pair shown in Figures 12 and 13. Panels a, b, and c of Figure 14 are images from Movie S2 (included in Supporting Information S1) prepared by the REGO project showing all sky camera views from Rankin Inlet projected geographically onto a map of the Hudson Bay region. The images are dominated by bright light from the moon (left) and the town (below), but these do not obscure the region of interest, located at the eastern edge of the image. The locations of CDR, SALU, PUVR, INUK, and KJPK near the eastern edge of Hudson Bay are shown by red crosses. Unfortunately, all are located just beyond the effective range of the Rankin Inlet camera. The aqua and purple boxes at the right show the magnetic footpoints of THEMIS D and E, mapped using the Tsyganenko-2001 (T01) magnetic field model. THEMIS D mapped to a location slightly west of INUK, and THEMIS E mapped to a location slightly east of PUVR.

Only very weak and featureless aurorae appeared near the four northern stations at 05:19 UT (panel a), before the start of the third GMD shown in Figures 12 and 13. At 05:26:30 UT (panel b), shortly before the time of the largest derivatives at CDR and SALU, a moderately bright east-west auroral region (orange) was evident at the eastern edge of the field of view to the west of those two stations. Movie S2, with images shown at a cadence of 15 s,

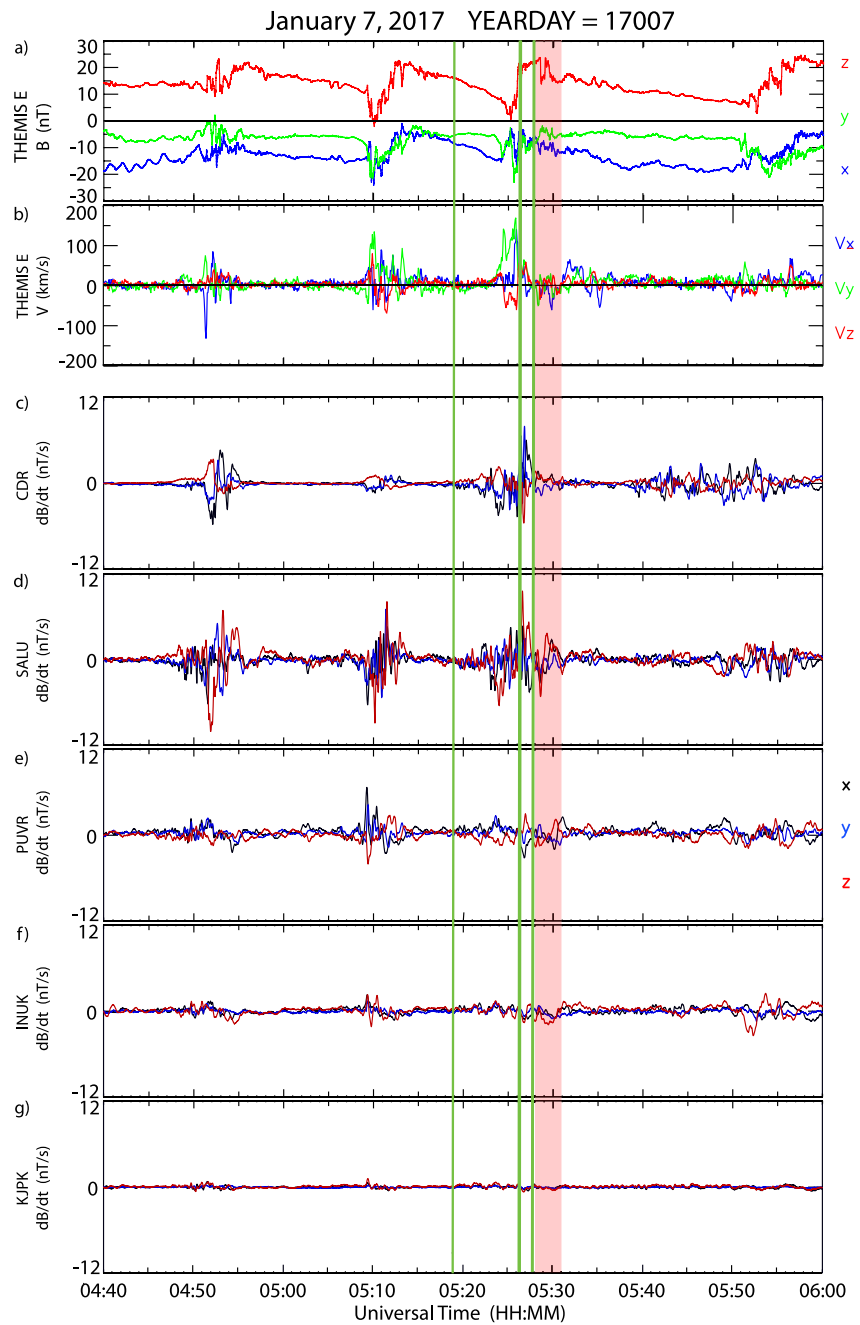


Figure 12. Composite plot showing simultaneous observations of the magnetic field and bulk velocity observed by THEMIS E and the magnetic field observed by five ground-based magnetometers, in order of decreasing latitude, from 04:40 to 06:00 UT 7 January 2017, as in Figure 4. Panels (c–g) show three components of the time derivative of the magnetic field from CDR, SALU, PUVR, INUK, and KJPK, respectively, in local geomagnetic coordinates. The vertical green lines correspond to the times of SECS maps and composite all-sky images shown in Figure 14, and the red shaded region corresponds to the time interval of the equatorward movement of an auroral streamer.

documents that it remained nearly stationary from the time of its first significant brightening at 05:26 until its later fading by 05:27 UT, and no auroral activity appeared in this region during the remainder of the movie (until 06:00 UT). At 05:28 UT (panel c), at the end of the GMD, only rather weak aurora with no discernible structure was evident near the four northern stations, and slightly more complex auroral arcs filled much of the region above the western half of Hudson Bay.

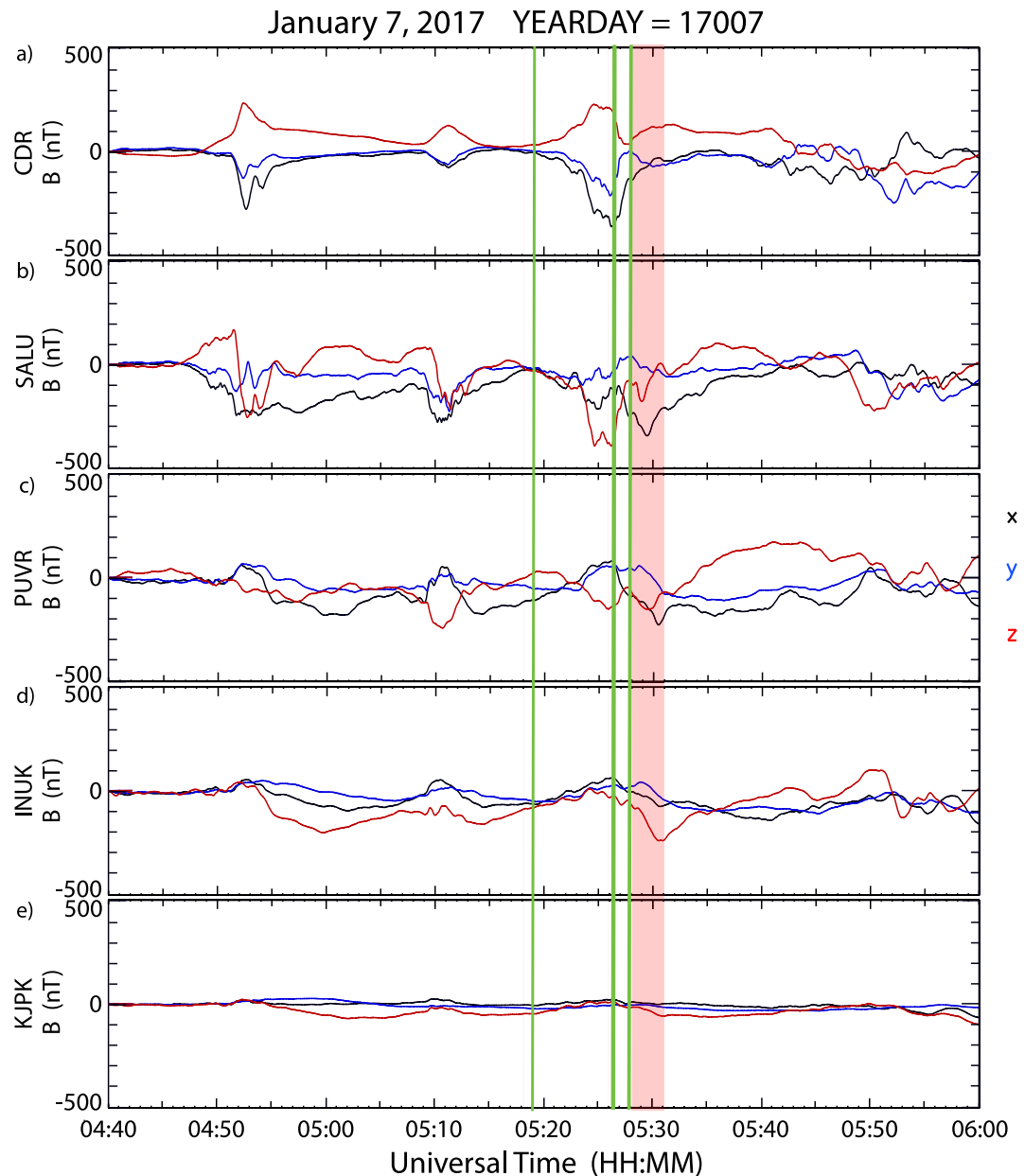


Figure 13. Composite plot showing the magnetic field observed by five ground-based magnetometers, in order of decreasing latitude, from 04:40 to 06:00 UT 7 January 2017, as in Figure 5. Panels (a–e) show three components of the magnetic field from CDR, SALU, PUVR, INUK, and KJPK, respectively, in local geomagnetic coordinates. The vertical green lines correspond to the times of SECS maps and composite all-sky images shown in Figure 14, and the red shaded region corresponds to the time interval of the equatorward movement of an auroral streamer.

Panels d, e, and f of Figure 14 are SECS maps of the equivalent ionospheric currents (black arrows) and vertical current intensities (upward in red, downward in blue) across northern North America. The stars show the locations of magnetometers providing data on this day, and the dots show grid points at which the currents were calculated. The yellow circle in each of these maps outlines the region of interest; the five stars it encloses correspond to the locations of the magnetometer stations. Panel d shows that at 05:19 UT, during an interval of very quiet magnetic activity before the GMD (Figure 12), there were almost no horizontal or vertical currents in this region. At 5:26:30 an intense, latitudinally localized upward current (red) appeared between CDR and SALU, a downward current (blue) extended from the northeast to the northwest of CDR, and a westward electrojet showed a counterclockwise

Table 3
Solar Wind, Interplanetary Magnetic Field, and Global Magnetic Activity Indices During Six Selected Days

Date	Time	IMF B	GSM IMF Bx	GSM IMF By	GSM IMF Bz	Vsw	Nsw	Psw	SML	SMU	SYM/H
12/26/2016	3:30:51	5.1	-2	4.5	-2.4	690	3.7	3.55	-314	133	-23
12/26/2016	5:17:35	5.3	-2.7	-1.3	-4	675	3.4	3.05	-239	79	-34
12/31/2016	4:46:47	5.7	-4.7	2.4	-1.6	310	16.5	3.05	-54	37	6
1/7/2017	4:53:31	3.8	-0.7	-1.9	-3.2	697	2.4	1.8	-199	53	-15
	5:11:11	4.0	-0.8	-3.4	-1.9	696	2.0	1.7	-174	55	-17
	5:26:58	4.8	-2.8	-3.7	-1.3	662	1.9	1.6	-240	182	-17
	4:51:27	4.0	-1.7	1.4	-3.3	707	2.8	2.0	-280	53	-14
	5:09:20	4.0	-1.6	-3.6	-0.7	693	1.7	1.7	-97	107	-17
	5:25:12	5.2	-2.1	-3.9	-2.8	689	2.4	1.9	-198	186	-17
1/19/2017	5:26:16	5.8	-2.7	4.5	1	600	3.9	2.8	-173	40	-24
	5:27:08	5.7	-2.5	4.4	1.2	593	3.9	2.7	-186	46	-24
1/27/2017	5:46:58	10.2	-7.7	1.7	6.2	631	6.8	5.4	-488	133	-16
	5:59:23	7.7	-2.7	3.4	2.1	637	6.8	5.5	-573	221	-19
	6:01:20	9.2	-3.5	2.5	6.7	629	6.7	5.3	-558	225	-19
2/5/2017	3:17:52	~6.1	~3	~-5.2	~-1.6	~500	~7	~2.9	-137	171	-21

Note. OMNI solar wind and IMF data were unavailable during 2-hr and 4-hr intervals surrounding the events on 7 January and 5 February 2017, respectively. Time-shifted ARTEMIS P2 data were substituted for 7 January, and time-shifted WIND data for 5 February and for Psw on 7 January.

vortical structure around CDR. By 5:28 UT the upward current had either moved or been replaced by a current at a position slightly northeast and southeast of SALU and beyond the range of the auroral imager, a latitudinally narrow westward electrojet appeared near SALU, and the region of downward current weakened and moved southward to just north of the electrojet. It is consistent with the lack of significant magnetic variations at INUK and KJPK, shown in the bottom panels of Figures 12 and 13, that GOES 13, with its magnetic footprint near Sanikiluaq, observed only steady levels of energetic electron fluxes and minor variations in the Hp magnetic field component during the entire time interval from 04:00 to 06:00 UT (not shown).

Figure 15 is a continuation of the sequence of SECS maps shown in Figure 14. The map in panel a is zoomed-in version of the map in Figure 14f at 05:28 UT, and panels b, c, and d show SECS maps in successive minutes from 05:29 to 05:31 UT. At 05:28 the localized upward current was eastward of SALU but extended both to the northeast and the northwest. By 05:29 UT this upward current was located southeast of SALU, remained in that position at 05:30 UT, and faded away by 05:31 UT. The vortical currents that pointed to the northwest immediately east of SALU and pointed to the southwest northwest of CDR at 05:26 UT were replaced by a single current that pointed to the northwest farther east of SALU at 05:28 UT, and at the same time the narrow westward electrojet from Greenland west through SALU reappeared in nearly linear form. The one northwest-pointing current at 05:28 pointed westward by 05:29 UT, and the latitudinally narrow westward electrojet persisted through 05:31 UT despite the fading away of the upward current that had been located south of SALU. The equatorward motion of the localized upward current region and the westward electrojet both indicate the presence and motion of a short-lived auroral streamer despite the absence of any direct evidence from an auroral imager.

4. Other Selected Events

Table 3 shows the values of the IMF in GSM coordinates, solar wind velocity (Vsw) in km/s, density (Nsw) in #/cm³, pressure (Psw) in nPa, and the SML, SMU, and SYM/H magnetic activity indices in nT for the nearly simultaneous DFB—GMD events on 6 days in 2016 and 2017. The IMF magnitude in all of these events only varied between 3.5 and 10.2 nT with a median of 4.4 nT, and the IMF Bz component varied between -4 and +3 nT, with a median of -1.1 nT. All but one event occurred during intervals of high (≥500 km/s) or very high (≥650 km/s) Vsw. OMNI data (not shown) indicated that these high Vsw intervals began from 1 to 3 days prior to

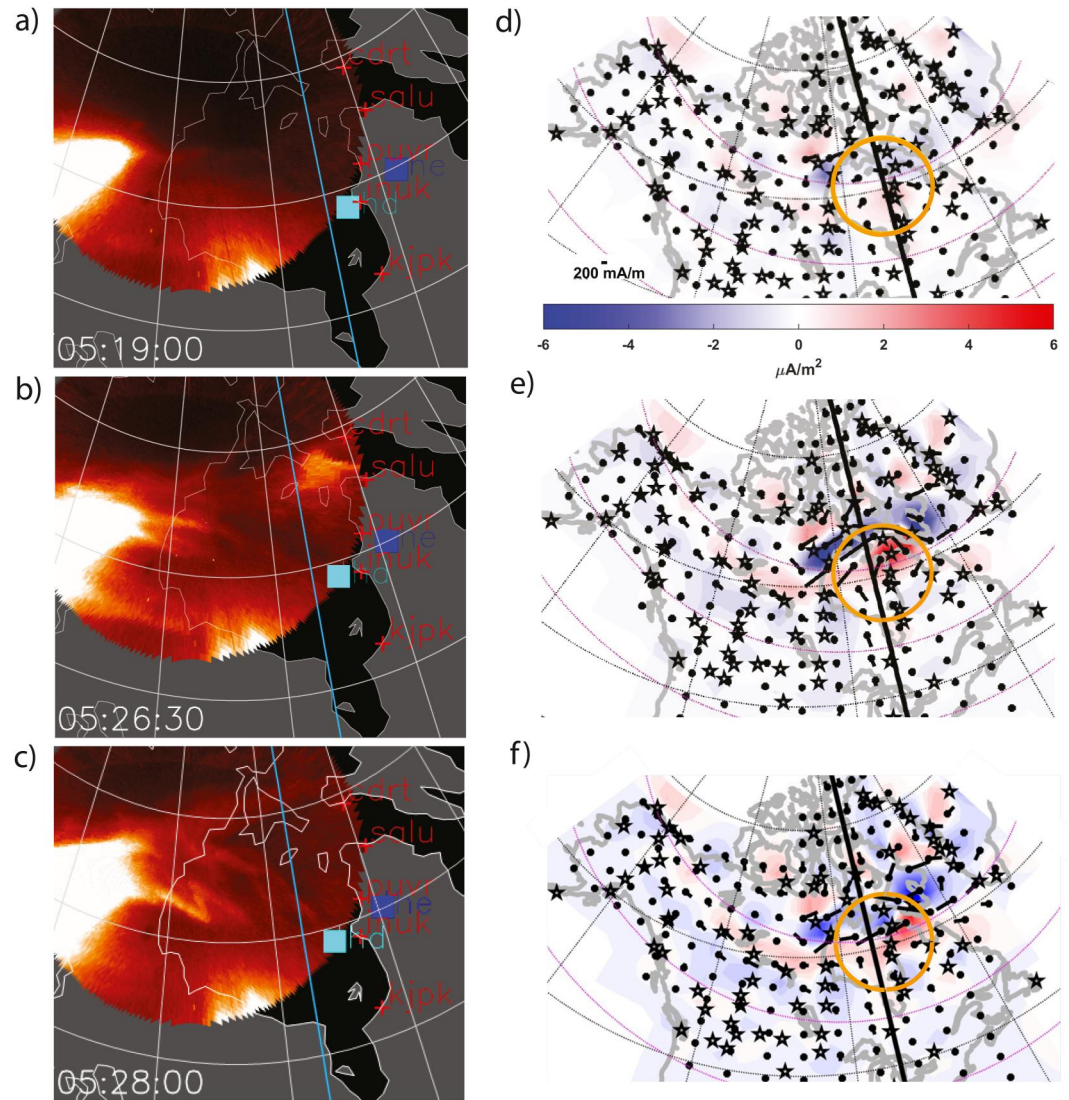


Figure 14. Composite all-sky auroral images and SECS maps as in Figures 6 and 7, but at 05:19, 05:26:30, and 05:28 UT on 7 January 2017.

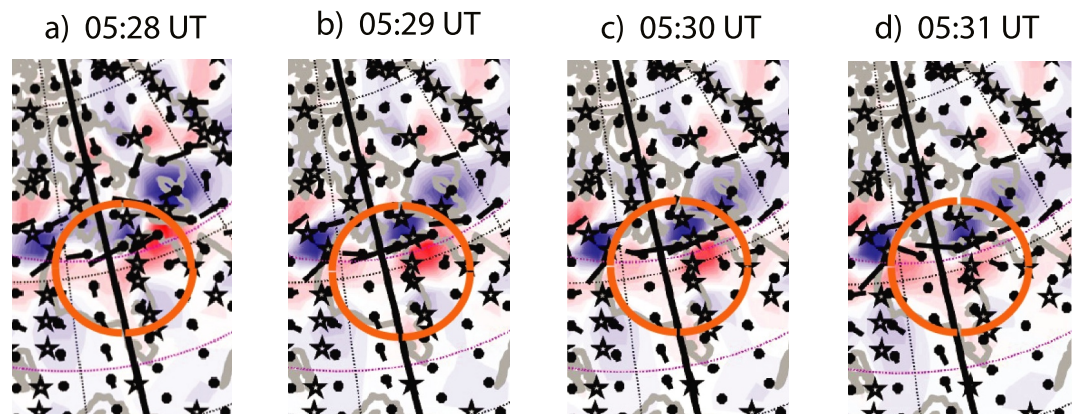


Figure 15. Zoomed-in SECS maps as in Figure 8, but at 05:28, 05:29, 05:30, and 05:31 UT on 7 January 2017.

Table 4
DFB and Near-Simultaneous GMD Event Times and DFB Locations and Velocities During Six Selected Days

Date	S/C	tDFB	tsGMD	tpGMD	V _x	V _y	X (R _E)	Y (R _E)	MLT
12/26/2016	A	3:30:51	3:30	3:32	5.4	3.9	-8.03	-0.12	0:03
12/26/2016	D	5:17:35	5:16	5:18	-4.2	10.7	-7.34	-1.55	0:43
12/31/2016	D	4:46:47	4:44	4:45	5	63.1	-7.17	-0.49	0:14
1/7/2017	D	4:53:31	4:51	4:52	-2.8	15.8	-7.69	0.08	23:58
	D	5:11:11	5:08	5:09	10	15.9	-7.94	-0.18	0:05
	D	5:26:58	5:23	5:27	1.2	25.5	-8.18	-0.43	0:11
	E	4:51:27	4:51	4:52	-8	21.3	-8.76	-1.08	0:25
	E	5:09:20	5:08	5:09	28.4	-6.5	-8.93	-1.35	0:31
1/19/2017	E	5:25:12	5:23	5:27	30.7	103.3	-9.08	-1.6	0:36
	D	5:26:16	5:25	5:27	39.4	46.3	-8.74	1.01	23:34
	E	5:27:08	5:25	5:27	108.6	84.2	-9.75	-0.02	0:01
1/27/2017	D	5:46:58	5:45	5:48	-28.4	-4.3	-9.31	1.77	23:20
	D	5:59:23	5:59	6:02	43.5	-45.4	-9.44	1.66	23:23
	E	6:01:20	5:59	6:02	-91.6	76.5	-10.4	0.66	0:46
2/5/2017	E	3:17:52	3:16	3:17	11.2	-23.6	-8.73	3.56	22:35

the DFBs. The only exception ($V_{sw} = 310$ km/s) occurred on 31 December 2016 in association with the only high value of N_{sw} (16.5 #/cc); no magnetic storm followed this event or closely preceded any of the other events. P_{sw} was low or modest in all cases. SML ranged from quiet to moderately disturbed (-54 to -573 nT), with a median of -199 nT. SMU also from ranged from quiet to moderately disturbed (37–225 nT), with a median of 68 nT, and SYM/H was consistently quiet, never dropping below -34 nT. These indicate intervals of strong magnetospheric driving (mainly by V_{sw}) but with little or moderate global magnetospheric response. We note, however, that the lack of any significant global response may be consistent with the generation of fewer DFBs, which might make the occurrence (and hence identification) of temporally and spatially isolated DFBs more likely.

Table 4 shows details of the DFB and GMD events listed in Table 3. Figures documenting each event and including information about substorm onsets near the time of these events (or not) are included in Supporting Information S1. Column 2 shows the time the dipolarization front was observed, column 3 shows tsGMD, the start time of the GMD, defined as the first minute showing an increased perturbation in one or more components of the magnetic field at one or more ground stations showing a large GMD, and column 4 shows tpGMD, the time of the peak derivative in any component of the GMD at one or more stations. Columns 5 and 6 show the GSM X and Y velocity components of the DFB, columns 7 and 8 show the GSM X and Y positions of the DFB, and column 9 shows its location in magnetic local time (MLT) in HH:MM.

Figure 16 shows the locations and velocities of each of the DFBs in Table 4 in the X-Y GSM plane. The DFBs were located between -7 and $-11 R_E$ in the $-X_{GSM}$ direction (tailward of Earth), and all but one were within $\pm 2 R_E$ and one hour MLT of the midnight meridian. The lines attached to each cross symbol show the direction and relative magnitude of the DFB velocity. The bulk velocity components were generally very small (less than 100 km/s), and much smaller than the ~ 300 km/s values noted by Runov et al. (2011). This may indicate that the DFBs were significantly decelerated and/or the probe was at a DFB flank and missed the DFB proper. The absolute values of V_x and V_y were also often close, which might signify a flankward flow deflection and/or vorticity. Indeed, it is evident in the summary plots that V_x and V_y often changed their signs, which indicates a flow vortex.

Although on 27 January 2017 both THEMIS probes D and E were located near the PSBL/lobe boundary and encountered a hot plasma sheet expansion at around 0600 UT, the velocities of the DFB observed by THEMIS E at 06:01 UT at $-10.4 R_E$, $1 R_E$ tailward of THEMIS D, did not at all follow the typical pattern in which DFBs have larger earthward velocities when they are observed at larger tailward distances. As shown in Figure S6 in Supporting Information S1, V_x was large and negative (at times exceeding -250 km/s) and V_y was positive and even larger (exceeding $+300$ km/s) during this DFB encounter. The phase delays between the V_x , V_y , and V_z

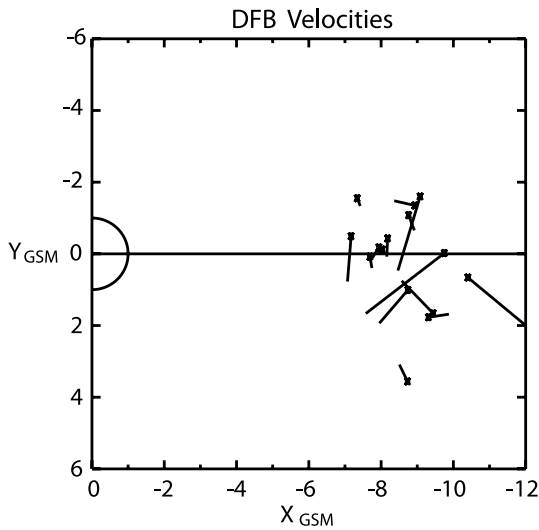


Figure 16. Plot of the locations and velocities of DFBs observed in the XY_{GSM} plane during near-simultaneous DFB—GMD events.

components indicate that THEMIS E encountered a sort of 3-D flow vortex, perhaps related to the passage of the spacecraft in, out, and back again into the plasma sheet. To put this anomalous event in perspective, we note that the DFB simulations shown in Figures 5 and 6 of Birn et al. (2019) included examples of vortex flows with large V_y components.

Figure 17 shows color-coded time delay values for the DFB-GMD events listed in Table 4. Figure 17a shows that the onset time of the GMD preceded the onset of the DFB by ≥ 2 min during eight of the 15 events, preceded it by 1.5 ± 0.5 min during four other events, and preceded it by < 1 min during three events. The mean time delay from GMD onset was 1.83 min and the standard deviation was 1.05 min. The events with larger time delay values generally were observed at X_{GSM} values nearer Earth and nearer local midnight, but with considerable scatter. Figure 17b is similar to Figure 17a, but time delays are from the time of the peak GMD derivative to DFB onset. For this time delay the peak time of the GMD preceded the onset of the DFB by ≥ 2 min during three of the 15 events, coincided in time to within ± 0.5 min during seven events, and followed the onset of the DFB during five events. That is, the peak GMD was approximately simultaneous with the time of the observation of the dipolarization front. The mean time delay from peak GMD was -0.23 min and the standard deviation was 1.31 min.

5. Discussion

Many previous studies have suggested that DFBs are causally related to magnetic disturbances observed by ground magnetometers, but most have focused on their possible contribution to substorm onsets and magnetic bays (Lyons et al., 2012) or global dipolarizations (first discussed by Baumjohann et al., 1999, exemplified in a multi-satellite study by Panov, Baumjohann, Nakamura, Weygand, et al. (2019) and a global magnetosphere MHD simulation by Merkin et al. (2019), and recently reviewed by Gabrielse et al., 2023), and very few have focused on their connection to short-lived but large amplitude GMDs. We note, however, that Ohtani et al. (2006), who compared GOES observations of dipolarization within 15 min of fast Earthward flows observed in the plasma sheet by the Geotail satellite, found that such fast flows were not always followed by ground substorm activity or geosynchronous dipolarization, and we have noted the observations of localized auroral and ionospheric current intensifications coincident with DFBs during non-substorm times reported by Jussola et al. (2009) and Panov, Baumjohann, Nakamura, Pritchett et al. (2019). This paper presents several examples of near-simultaneous DFBs observed by THEMIS spacecraft in the near magnetotail and spatially isolated and temporally localized large amplitude GMDs observed by multiple ground magnetometers located along the east and

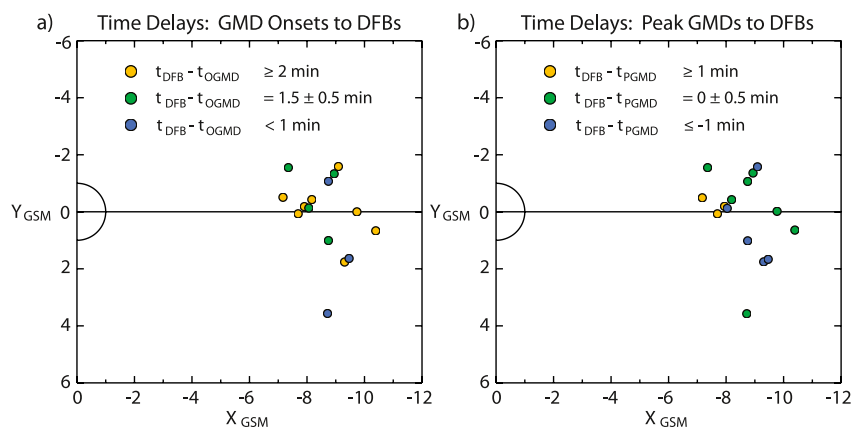


Figure 17. (a) The time difference between the time of GMD onsets and DFBs, and (b) The time difference between the time of the peak GMD derivatives and DFBs, respectively, for the events listed in Table 4.

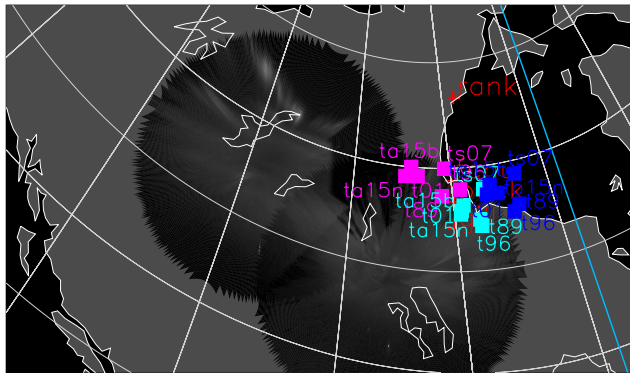


Figure 18. An auroral image similar to Figure 6a for 05:44 UT 27 January 2017, but with the magnetic field footprints of THEMIS A (pink), D (aqua), and E (blue) and of various magnetic field models superposed: T89, T96, T01, TS07, TA15B, and TA15N.

FCHU (near the west coast of Hudson Bay) and INUK (on the east coast of Hudson Bay) and the values of the full-width half maximum radii of GMDs of ~ 275 km reported by Engebretson, Pilipenko, et al. (2019) and 250–450 km reported by Weygand et al. (2021). For the two events presented in Section 3, we used the Tsyanenko T01 magnetic field model (Tsyanenko, 2002a, 2002b), which included as inputs a “trail” of 5-min averages of the IMF, solar wind, and *Dst* field data, covering the preceding 2-hr interval. The T01 model is known to give more accurate footprints than T89 (e.g., Nishimura et al., 2011) and our results indicated good agreements between the THEMIS footprints and the ground stations showing the largest GMDs (Figures 5, 6, and 11).

Figures 18 and 19 show the results of applying the methods of Nishimura et al. (2011) to several different magnetic field models to estimate the mapping uncertainty considering various ways in which these models depend on the magnetic field geometry and solar wind history. Figure 18 shows an auroral image similar to Figure 6a for 05:44 UT 27 January 2017, but with the magnetic field footprints of THEMIS A, D, and E of various magnetic field models superposed: T89, T96 (Tsyanenko, 1995), T01 (Tsyanenko, 2002a, 2002b), TS07 (Tsyanenko & Sitnov, 2007), TA15B (Tsyanenko & Andreeva, 2015a), and TA15N (Tsyanenko & Andreeva, 2015b). The footprints for all the models are clustered to a ~ 200 km region for each satellite. Figure 19 shows an auroral image similar to Figure 14a for 05:19 UT 7 January 2017, but with the magnetic field footprints of THEMIS D and E of the above six magnetic field models superposed. The footprints for all of the models are clustered to a small region. The latitude uncertainty may be ~ 200 km for each satellite but the longitude uncertainty is 50 km or less. These levels of uncertainty would not affect the conclusions of this study.

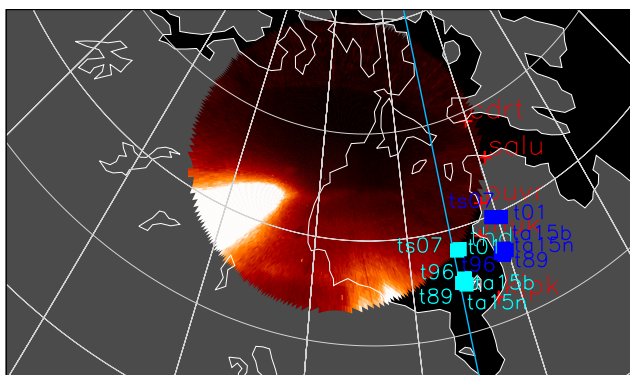


Figure 19. An auroral image similar to Figure 14a for 05:19 UT 7 January 2017, but with the magnetic field footprints of THEMIS D (aqua) and E (blue) and of various magnetic field models superposed: T89, T96, T01, TS07, TA15B, and TA15N.

west coast of Hudson Bay, Canada. We have also noted the appearance of weaker GMDs slightly farther west of Hudson Bay that were not observed by the THEMIS spacecraft. Several issues needed to be addressed in order to identify useful events and gain confidence that the DFBs and GMDs are causally related.

First, mapping of magnetic field lines from the near tail to the ground continues to be generally challenging, as empirical models are parameterized by only a few global variables. We addressed this issue by first mapping the northern hemisphere footprint of the THEMIS spacecraft using the Tsyanenko model T89 (Tsyanenko, 1989) via the SSCWEB utility and selecting any event for which that footprint was located in eastern Arctic Canada, from ~ 300 km west of Hudson Bay to the east coast of Labrador. We then looked at ground magnetometer data from the stations shown in Figure 1 to identify large GMDs that occurred near the time of the DFBs. We found that events with footprints far to the west or east of Hudson Bay did not correspond to any near-simultaneous GMD, and those events with footprints near the middle of Hudson Bay corresponded to either no events or only weak events.

These results are consistent with the 923 km separation distance between FCHU (near the west coast of Hudson Bay) and INUK (on the east coast of Hudson Bay) and the values of the full-width half maximum radii of GMDs of ~ 275 km reported by Engebretson, Pilipenko, et al. (2019) and 250–450 km reported by Weygand et al. (2021). For the two events presented in Section 3, we used the Tsyanenko T01 magnetic field model (Tsyanenko, 2002a, 2002b), which included as inputs a “trail” of 5-min averages of the IMF, solar wind, and *Dst* field data, covering the preceding 2-hr interval. The T01 model is known to give more accurate footprints than T89 (e.g., Nishimura et al., 2011) and our results indicated good agreements between the THEMIS footprints and the ground stations showing the largest GMDs (Figures 5, 6, and 11).

Second, what relative timing might be expected between DFBs and GMDs? The earthward velocity of DFBs deeper in the magnetotail, averaging 300 km/s near $X_{GSM} = -15 R_E$, dropped to an average of 180 km/s near $X_{GSM} = -8 R_E$ (Figure 4b of Liu et al., 2014). Braking of the DFB in the transition region ($X_{GSM} \geq -10 R_E$) reduces this earthward velocity, sometimes even stopping (Sergeev et al., 2014) or reversing it, and in the process generates a field aligned current pair. These can rapidly travel toward the ionosphere to drive the magnetic and auroral signatures observed. The braking process is not instantaneous; momentum is transferred throughout the deceleration. The buildup of plasma ahead of the dipolarization front as the DFB moves earthward has been well documented (Runov et al., 2011). The events listed in Section 4 all show the initiation of a GMD ~ 2 min before the observation of the dipolarization front, with a tendency to occur with a larger lead time for events observed nearer Earth—and thus later in the deceleration process. The time delay and its dependence on spacecraft position downtail reported here are therefore consistent with what is known of the braking process.

Third, even though the number of spacecraft in the braking region is quite limited, it is known that many DFBs can occur in a short time interval at slightly different locations. How can one be confident that a given DFB and GMD are related? In particular, what are the typical scale sizes of DFBs, and how do these map to the ground? We use the T01 magnetic field model to address a related inverse question: how does a given set of locations on the ground map to the braking region?

Figure 20 shows the results of mapping a set of five ground locations (BACK and 50 km N, S, E, and W of it) to the GSM X distance tailward where THEMIS D observed a DFB at 5:59 UT 27 January 2017, using the T01 magnetic field model. The cross and diamond symbols in Figure 20a show these five locations, respectively, near the southwest corner of Hudson Bay. Figure 20b shows a mapped projection of the magnetic field lines through these five ground locations on a GSM Z-X grid tailward from the northern ionosphere to the neutral sheet and earthward again toward the southern ionosphere. The location of THEMIS D, shown by the black square, is south of the neutral sheet at $X_{\text{GSM}} = -9.43 R_E$ and $Z_{\text{GSM}} = -3.75 R_E$, adjacent to the mapped field line locations south of the neutral sheet near this same X_{GSM} distance. Figure 20c shows a zoomed-in view of the Z_{GSM} and Y_{GSM} locations of THEMIS D and these mapped field lines south of the neutral sheet at this same X_{GSM} distance.

Table 5 presents the Y_{GSM} and Z_{GSM} coordinates of these mapped magnetic field lines at $X_{\text{GSM}} = -9.43 R_E$, the distances of the N, S, E, and W field lines in R_E and km from the mapped BACK field line, and dimensionless mapping factors determined as the ratio between these distances and 50 km.

Liu, Angelopoulos, Zhou, et al. (2013) used two methods to infer the radius of DFBs using a data set of 472 earthward traveling DFBs observed by THEMIS spacecraft and concluded that although the radii varied from event to event and could occasionally reach $3 R_E$, their median radius was $0.8\text{--}1.0 R_E$. It is not yet known whether the transverse extent of field-aligned currents induced during DFB braking preserves this radius or expands as they are transmitted earthward. Assuming that this radius is preserved, the mean mapping factors of ~ 32 for longitudinal separations and 62.5 for latitudinal separations together with the median radius of DFBs ($0.9 R_E = 5,734$ km) give estimates of the median radius of DFBs mapped to the ionosphere of 180 km in east-west extent and 90 km in north-south extent. These values are smaller than but of the same order of magnitude as the extent of the localized field-aligned currents shown in Figures 6–8, 14 and 15, and roughly half of the half amplitude radii of GMDs cited above. Because the sensitivity of ground magnetometers to currents in the ionosphere falls off only gradually with horizontal distances of ~ 100 km, however, we consider the mapped DFB radii and half amplitude GMD radii to be in reasonable agreement.

Fourth, although we are confident that in each of the examples shown a DFB observed at a THEMIS spacecraft is related to a GMD observed nearly simultaneously at two or more closely spaced ground magnetometer stations, the available data do not allow us to conclude that any given GMD is related to a DFB. Because DFB observations are local measurements made by at most a few spacecraft as they pass through the near tail, DFBs at other local times and possibly at higher L shells will not be observed. In the case of January 27, no DFBs were observed while the satellites' footprints mapped to regions overhead and to the west of the GOES 14 footprint, so it is probable but not certain that no relevant DFBs existed.

Fifth, we have noted that short-lived stationary auroral regions and/or streamers and intense GMDs occurred in association with highly localized upward and downward field aligned current pairs shortly before and during each DFB, the resulting short-lived electrojet between them was narrow, and the surrounding horizontal currents were relatively weak compared to the electrojet currents observed during non-GMD times. In contrast, the auroral streamers and weaker GMDs to the west of the Churchill line on January 27 appeared when the separation between the upward and downward currents was larger, the electrojet currents were stronger and more extended, and the level of background auroral activity was higher.

Finally, despite the observations reported here and earlier, the physics underlying the physical pathways from DFBs to GMDs is currently only qualitatively understood. Both rapid temporal magnetic field variations and the motion of highly localized spatial variations will result in dB/dt observations in ground magnetometer data at fixed locations. In our earlier study of GMDs at conjugate sites in Greenland and Antarctica Engebretson et al. (2020), following Apatenkov et al. (2020), noted that the magnetic field created by ionospheric and magnetospheric currents may vary due to both temporal changes of current amplitudes and to the motion of the current structures. The total time derivative dB/dt observed on the ground is $\text{dB}/\text{dt} = \partial\mathbf{B}/\partial t + (\mathbf{V} \cdot \nabla)\mathbf{B}$. Although

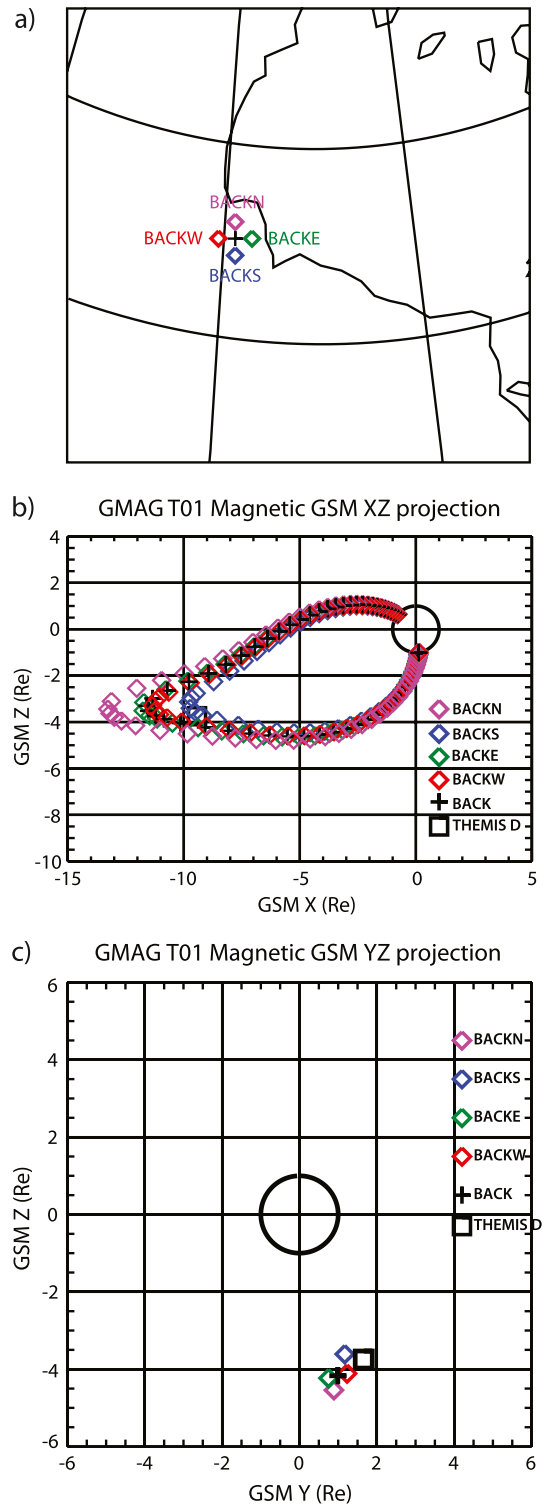


Figure 20. (a) Map of the region near the southwest corner of Hudson Bay, Canada showing the location of BACK (cross) and locations 50 km north (BACKN), south (BACKS), west (BACKW) and east (BACKE) of BACK (colored diamonds). (b) Traces of the mapped magnetic field lines from these five locations (cross and diamonds) in a GSM Z-X grid tailward from the northern ionosphere to the neutral sheet and earthward again toward the southern ionosphere. The GSM Z-X location of THEMIS D (black square) is also shown. (c) Plots of the Z_{GSM} and Y_{GSM} locations of THEMIS D and these mapped field lines south of the neutral sheet at a tailward distance of $X_{GSM} = -9.43 R_E$.

Table 5

Mapped Locations in GSM Coordinates of Magnetic Field Lines From 50 km N, S, E, and W of BACK to the X_{GSM} Location of THEMIS D at 5:59 UT 27 January 2017, Distance Between the Mapped N, S, E, and W Field Lines and the Location of the Mapped BACK Field Line, and the Resulting Ground-To Space Mapping Factors

Station	N		S		E		W		BACK	
	Y	Z	Y	Z	Y	Z	Y	Z	Y	Z
Locations (R_E)	0.89	-4.54	1.17	-3.61	0.75	-4.23	1.23	-4.11	0.99	-4.17
Distance to BACK (R_E)	0.384		0.600		0.245		0.253		0	
Distance to BACK (km)	2452		3,802		1,561		1,609		0	
Scale mapping factors	49.0		76.0		31.2		32.2		-	

the application of this realization in these two papers was to GMDs produced by omega bands, we consider it to be possible that the rapid onset and decay of the localized field-aligned currents generated by DFBs in a region of relatively low auroral activity (and low conductivity) may generate similarly moving but very localized current structures.

6. Summary and Conclusions

1. As a result of surveying days in 2015–2017 when the apogees of THEMIS A, D, and E were in the midnight sector, one or more DFBs occurred, and the footpoint of the spacecraft's magnetic field in the northern ionosphere were in the longitudinal region surrounding Hudson Bay, we identified 6 days during which one or more of these DFBs spacecraft coincided closely in time with ≥ 6 nT/s GMDs, observed by latitudinally closely spaced magnetometers near the west or east coasts of Hudson Bay. When the spacecraft were over the middle of Hudson Bay or far to the west or east of it, little or no GMD activity was observed at these ground stations. This is consistent with the results of mapping the spatial extent of DFBs to the ionosphere using the T01 magnetic field model and with our previous observations of the longitudinal extent of GMDs.
2. On two of these days we showed auroral imager data and SECS maps of ionospheric and vertical currents, in each case showing a quiet interval before the DFB and GMD, a disturbed interval during the events, and another quiet or nearly quiet interval after the event. In each case the footpoints of two THEMIS spacecraft were very near the ground stations, and a localized intense upward and downward current pair, a vortical perturbation of a westward electrojet, and an auroral intensification and/or streamers appeared during the DFB and GMD and disappeared thereafter. These several simultaneous features are consistent with the observations of the auroral drivers of large dB/dt events by Ngwira et al. (2018), Engebretson, Pilipenko, et al. (2019), and Engebretson, Steinmetz, et al. (2019).
3. Increased levels of energetic electron fluxes observed by GOES 14 shortly after each of the DFB - GMD events on January 27 were consistent with nearby auroral activity. During the first event the fluxes were spatially and temporally independent of the GMD, but they appeared to be related to the wider longitudinal extent of the auroras associated with the second event.
4. All but one of the DFB—GMD pairs during these 6 days occurred under elevated V_{sw} and low N_{sw} and P_{sw} conditions (most above 600 km/s and below 4 cm^{-3} and 3 nPa, respectively). The SYM/H index was above -25 nT for all but one event. The SML and SMU indices showed activity ranging from quiet through moderately disturbed. These external conditions, along with the close temporal association of some but not all of these events with substorm onsets, indicates that they occurred during HILDCAA events, and with essentially no relation to any magnetic storms.
5. GMD onsets during these 6 days began ~ 2 min before the time of DFB observation, and GMD peaks occurred nearly simultaneously with them. These time differences most likely reflect the fact that a region of increased plasma pressure typically precedes a DF by 1 min.
6. The earthward velocity (V_x) of the DFBs observed during these 6 days, at locations in X_{GSM} between -7 and $-11 R_E$, was with two exceptions lower for events nearer Earth. This is consistent with other DFB observations, and is attributed to braking of the DFBs. The slight increase in the time difference between GMD onsets and DFs observed nearer Earth appears to reflect the fact that the braking of the DFB is not instantaneous: information on the braking may begin to be transferred via field aligned currents and electron precipitation as braking begins but continues as the DFB comes nearer Earth.

- Additional observations of GMDs and DFBs are certainly warranted, especially in regions with not only dense magnetometer coverage but also with more complete coverage by auroral imagers. We hope, however, that the observations reported here will stimulate modelers to increase their focus on DFBs occurring not only during storm times or the times of substorm onsets, but also during times when large, isolated GMDs occur.

Data Availability Statement

Ground-based magnetometer data used in this study were recorded at stations in the MACCS (Engebretson et al., 2011), AUTUMNX (Connors et al., 2016), CARISMA (Mann et al., 2023), and CANMOS (Calp, 2023) arrays in Eastern Arctic Canada. AUTUMNX data are available from the CDAWEB site (Papatashvili & King, 2020). The SuperMAG SML and SMU indices accessed in this study are available from the SuperMAG web site (Gjerloev, 2023). THEMIS satellite data, THEMIS all sky imager data, and THEMIS ground-based magnetometer data are available from the THEMIS web site (Angelopoulos, 2022; Mende, 2004; Russell, 2004). REGO all sky imager data are available from the GO-Canada REGO web site (Donovan, 2014). The GOES-13 and -14 data are available from the NOAA National Centers for Environmental Information (NCEI) (NOAA, 2020, 2023). FORTRAN Source code for all Tsyganenko empirical magnetosphere models can be accessed at Tsyganenko (2022). The Tsyganenko T01 model implementation in IDL (GEOPACK) used in this study was developed by Korth (2020). Field line tracing modules used were accessed via the Space Physics Environment Data Analysis System (SPEDAS) IDL Geopack Library (SPEDAS, 2023).

Acknowledgments

This research was supported by NSF Grant AGS-2013648 to Augsburg University and AGS-2013433 to the University of Michigan. Work at the Space Science Institute was supported by NSF Grant AGS-2027210 and NASA Grant 80NSSC19K0907. Work at UCLA by AR was supported by NASA-LWS Grant 80NSSC20K1788, and work by JMW was supported by NASA Grants 80NSSC18K0570 and 80NSSC18K1220 and NSF Grant AGS-2013648 via subcontract from Augsburg University. Work at Virginia Tech was supported by NSF Grants OPP-1744828 and AGS-2027168 and NASA Grant 19-LWS19_2-0043. The work of YN was supported by NASA Grants 80NSSC20K0725, 80NSSC21K1321, 80NSSC22K0323, 80NSSC22K0749 and 80NSSC23K0410, NSF Grants AGS-1907698 and AGS-2100975, and AFOSR Grants FA9550-23-1-0614 and FA9550-23-1-0634. The research at the University of Colorado was supported by NOAA cooperative agreements NA17OAR4320101 and NA22OAR4320151. MGC thanks NSERC for research support and the Canadian Space Agency for support of AUTUMNX. IRM was supported by the Natural Sciences and Engineering Research Council of Canada. We thank Ian Mann, D. K. Milling, A. Kale and the rest of the CARISMA team for data. CARISMA is operated by the University of Alberta, funded by the Canadian Space Agency. We acknowledge NASA contract NAS5-02099 and V. Angelopoulos for use of data from the THEMIS Mission; C.W. Carlson and J.P. McFadden for use of ESA data; and D. Larson and R. P. Lin for use of SST data. THEMIS FGM data were provided under the lead of the Technical University of Braunschweig and with financial support through the German Ministry for Economy and Technology and the German Center for Aviation and Space (DLR) under contract 50 OC 0302. The THEMIS and REGO all-sky imagers are supported by NASA NAS5-02099 and the Canada Foundation for Innovation, respectively. We gratefully acknowledge the SuperMAG collaborators (<http://supermag.jhuapl.edu/info/?page=acknowledgement>). Jesper Gjerloev is SuperMAG Principal Investigator.

References

Amm, O., & Viljanen, A. (1999). Ionospheric disturbance magnetic field continuation from the ground to the ionosphere using spherical elementary currents systems. *Earth Planets and Space*, 51(6), 431–440. <https://doi.org/10.1186/BF03352247>

Angelopoulos, V. (2008). The THEMIS mission. *Space Science Reviews*, 141(1–4), 5–34. <https://doi.org/10.1007/s11214-008-9336-1>

Angelopoulos, V. (2022). THEMIS satellite level 2 data [Dataset]. *University of California*. Retrieved from http://themis.ssl.berkeley.edu/overview_data.shtml

Angelopoulos, V. (2023). GITHUB IDL_GEOPACK library [Software]. https://github.com/spedas-j/spedas_watch/blob/master/idl/external/IDL_GEOPACK/trace/trace2iono.pro

Angelopoulos, V., Baumjohann, W., Kennel, C. F., Coroniti, F. V., Kivelson, M. G., Pellat, R., et al. (1992). Bursty bulk flows in the inner central plasma sheet. *Journal of Geophysical Research*, 97(A4), 4027–4039. <https://doi.org/10.1029/91JA02701>

Angelopoulos, V., Coroniti, F. V., Kennel, C. F., Kivelson, M. G., Walker, R. J., Russell, C. T., et al. (1996). Multipoint analysis of a bursty bulk flow event on April 11, 1985. *Journal of Geophysical Research*, 101(A3), 4967–4989. <https://doi.org/10.1029/95JA02722>

Angelopoulos, V., Kennel, C. F., Coroniti, F. V., Pellat, R., Kivelson, M. G., Walker, R. J., et al. (1994). Statistical characteristics of bursty bulk flow events. *Journal of Geophysical Research*, 99(A11), 21257–21280. <https://doi.org/10.1029/94JA01263>

Apatenkov, S. V., Piliipenko, V. A., Gordeev, E. I., Viljanen, A., Juusola, L., Belakhovsky, V. B., et al. (2020). Auroral omega bands are a significant cause of large geomagnetically induced currents. *Geophysical Research Letters*, 47(6), e2019GL086677. <https://doi.org/10.1029/2019GL086677>

Auster, H. U., Glassmeier, K. H., Magnes, W., Aydogar, O., Baumjohann, W., Constantinescu, D., et al. (2008). The THEMIS fluxgate magnetometer. *Space Science Reviews*, 141(1–4), 235–264. <https://doi.org/10.1007/s11214-008-9365-9>

Baumjohann, W., Hesse, M., Kokubun, S., Mukai, T., Nagai, T., & Petrukovich, A. A. (1999). Substorm dipolarization and recovery. *Journal of Geophysical Research*, 104(A11), 24995–25000. <https://doi.org/10.1029/1999JA90028224995-25000>

Baumjohann, W., Paschmann, G., & Cattell, C. A. (1989). Average plasma properties in the central plasma sheet. *Journal of Geophysical Research*, 94, 6597–6606. <https://doi.org/10.1029/JA094iA06p06597>

Baumjohann, W., Paschmann, G., & Lühr, H. (1990). Characteristics of high-speed ion flows in the plasma sheet. *Journal of Geophysical Research*, 95, 3801–3809. <https://doi.org/10.1029/JA095iA04p03801>

Birn, J., Liu, J., Runov, A., Kepko, L., & Angelopoulos, V. (2019). On the contribution of dipolarizing flux bundles to the substorm current wedge and to flux and energy transport. *Journal of Geophysical Research: Space Physics*, 124(7), 5408–5420. <https://doi.org/10.1029/2019JA026658>

Califf, S., Rich, F. J., Loto'aniu, T. M., Singer, H. J., & Redmon, R. J. (2023). Long-term bias stability of the GOES-NOP magnetometers. *Earth and Space Science*, 10(11), e2023EA003035. <https://doi.org/10.1029/2023EA003035>

Calp, D. (2023). Canadian magnetic observatory system (CANMOS) data [Dataset]. *Natural Resources Canada*. Retrieved from <http://geomag.nrcan.gc.ca/data-donnee/sd-en.php>

Connors, M., Schofield, I., Reiter, K., Chi, P. J., Rowe, K. M., & Russell, C. T. (2016). The AUTUMNX magnetometer meridian chain in Quebec, Canada. *Earth Planets and Space*, 68(2), 2. <https://doi.org/10.1186/s40623-015-0354-4>

Donovan, E. (2014). REGO all sky imager data [Dataset]. *University of Calgary, Canada*. Retrieved from https://data.phys.ucalgary.ca/sort_by_instrument/all_sky_camera/GO-Canada_REGO/stream0

Donovan, E., Mende, S. B., Jackel, B., Frey, H. U., Syrjäsoo, M., Voronkov, I., et al. (2006). The THEMIS all-sky imaging array—System design and initial results from the prototype imager. *Journal of Atmospheric and Solar-Terrestrial Physics*, 68(13), 1472–1487. <https://doi.org/10.1016/j.jastp.2005.03.027>

Dubyagin, S., Sergeev, V., Apatenkov, S., Angelopoulos, V., Nakamura, R., McFadden, J., et al. (2010). Pressure and entropy changes in the flow-braking region during magnetic field depolarization. *Journal of Geophysical Research*, 115(A10), A10225. <https://doi.org/10.1029/2010JA015625>

Engebretson, M., Steinmetz, E., & Moldwin, M. (2011). MACCS 0.5 s ground magnetometer data [Dataset]. *Augsburg University*. <https://doi.org/10.48322/syjd-ab90>

- Engebretson, M. J., Ahmed, L. Y., Pilipenko, V. A., Steinmetz, E. S., Moldwin, M. B., Connors, M. G., et al. (2021). Superposed epoch analysis of nighttime magnetic perturbation events observed in Arctic Canada. *Journal of Geophysical Research: Space Physics*, *126*(9), e2021JA029465. <https://doi.org/10.1029/2021JA029465>
- Engebretson, M. J., Hughes, W. J., Alford, J. L., Zesta, E., Cahill, L. J., Jr., Arnoldy, R. L., & Reeves, G. D. (1995). Magnetometer array for cusp and cleft studies observations of the spatial extent of broadband ULF magnetic pulsations at cusp/cleft latitudes. *Journal of Geophysical Research*, *100*(A10), 19371–19386. <https://doi.org/10.1029/95JA00768>
- Engebretson, M. J., Kirkevold, K. R., Steinmetz, E. S., Pilipenko, V. A., Moldwin, M. B., McCuen, B. A., et al. (2020). Interhemispheric comparisons of large nighttime magnetic perturbation events relevant to GICs. *Journal of Geophysical Research: Space Physics*, *125*(8), e2020JA028128. <https://doi.org/10.1029/2020JA028128>
- Engebretson, M. J., Pilipenko, V. A., Ahmed, L. Y., Posch, J. L., Steinmetz, E. S., Moldwin, M. B., et al. (2019). Nighttime magnetic perturbation events observed in Arctic Canada: 1. Survey and statistical analysis. *Journal of Geophysical Research: Space Physics*, *124*(9), 7442–7458. <https://doi.org/10.1029/2019JA026794>
- Engebretson, M. J., Pilipenko, V. A., Steinmetz, E. S., Moldwin, M. B., Connors, M. G., Boteler, D. H., et al. (2021). Nighttime magnetic perturbation events observed in Arctic Canada: 3. Occurrence and amplitude as functions of magnetic latitude, local time, and magnetic disturbances. *Space Weather*, *19*, e2020SW002526. <https://doi.org/10.1029/2020SW002526>
- Engebretson, M. J., Steinmetz, E. S., Posch, J. L., Pilipenko, V. A., Moldwin, M. B., Connors, M. G., et al. (2019). Nighttime magnetic perturbation events observed in Arctic Canada: 2. Multiple-Instrument observations. *Journal of Geophysical Research: Space Physics*, *124*(9), 7459–7476. <https://doi.org/10.1029/2019JA026797>
- Engebretson, M. J., Yang, L., Steinmetz, E. S., Pilipenko, V. A., Moldwin, M. B., McCuen, B. A., et al. (2024). Extreme geomagnetic disturbances (GMDs) observed in eastern Arctic Canada: Occurrence characteristics and solar cycle dependence. *Journal of Geophysical Research: Space Physics*, *129*(1), e2023JA031643. <https://doi.org/10.1029/2023JA031643>
- Forsyth, C., Rae, I. J., Coxon, J. C., Freeman, M. P., Jackman, C. M., Gjerloev, J., & Fazakerley, A. N. (2015). A new technique for determining substorm onsets and phases from indices of the electrojet (SOPHIE). *Journal of Geophysical Research: Space Physics*, *120*(12), 10592–10606. <https://doi.org/10.1002/2015JA021343>
- Forsyth, C., Sergeev, V. A., Henderson, M. G., Nishimura, Y., & Gallardo-Lacourt, B. (2020). Physical processes of meso-scale, dynamic auroral forms. *Space Science Reviews*, *216*(46), 46. <https://doi.org/10.1007/s11214-020-00665-y>
- Gabrielse, C., Gkioulidou, M., Merkin, S., Malaspina, D., Turner, D. L., Chen, M. W., et al. (2023). Mesoscale phenomena and their contribution to the global response: A focus on the magnetotail transition region and magnetosphere-ionosphere coupling. *Frontiers in Astronomy and Space Science*, *10*, 1151339. <https://doi.org/10.3389/fspas.2023.1151339>
- Gjerloev, J. W. (2023). SuperMAG, Global magnetic field observations and products made possible by the contributors [Dataset]. *Applied Physics Laboratory*. Retrieved from <https://supermag.jhuapl.edu/>
- Hanser, F. (2011). *EPS/HEPAD calibration and data handbook*. Assurance Technology Corporation. Retrieved from https://www.ngdc.noaa.gov/stp/satellite/goes/doc/goes_nop/GOESN-ENG-048_RevD_EPS_HEPAD_13May2011.pdf
- Jaynes, A. N., Lessard, M. R., Rodriguez, J. V., Donovan, E., Loto'aniu, T. M., & Rychert, K. (2013). Pulsating auroral electron flux modulations in the equatorial magnetosphere. *Journal of Geophysical Research: Space Physics*, *118*(8), 4884–4894. <https://doi.org/10.1002/jgra.50434>
- Juusola, L., Nakamura, R., Amm, O., & Kauristie, K. (2009). Conjugate ionospheric equivalent currents during bursty bulk flows. *Journal of Geophysical Research*, *114*(A4), A04313. <https://doi.org/10.1029/2008JA013908>
- Kauristie, K., Sergeev, V. A., Pulkkinen, T. I., Pellinen, R. J., Angelopoulos, V., & Baumjohann, W. (1996). Study on the ionospheric signatures of the plasma sheet bubbles. In *Third International Conference on Substorms, (ICS-3), ESA SP-389* (pp. 93–98).
- Korth, H. (2020). IDL GEOPACK dynamic link module: April 8, 2020 release (version 10.6) [Software]. *Applied Physics Laboratory*. Retrieved from <https://ampere.jhuapl.edu/tools/>
- Li, S.-S., Angelopoulos, V., Runov, A., Zhou, X.-Z., McFadden, J. P., Larson, D., et al. (2011). On the force balance around dipolarization fronts within bursty bulk flows. *Journal of Geophysical Research*, *116*(A5), A00135. <https://doi.org/10.1029/2010JA015884>
- Liu, J., Angelopoulos, V., Runov, A., & Zhou, X.-Z. (2013). On the current sheets surrounding dipolarizing flux bundles in the magnetotail: The case for wedgelets. *Journal of Geophysical Research: Space Physics*, *118*(5), 2000–2020. <https://doi.org/10.1002/jgra.50092>
- Liu, J., Angelopoulos, V., Zhang, X.-J., Runov, A., Artemyev, A., Plaschke, F., et al. (2017). Ultralow frequency waves deep inside the inner magnetosphere driven by dipolarizing flux bundles. *Journal of Geophysical Research: Space Physics*, *122*(10), 10112–10128. <https://doi.org/10.1002/2017JA024270>
- Liu, J., Angelopoulos, V., Zhou, X.-Z., & Runov, A. (2014). Magnetic flux transport by dipolarizing flux bundles. *Journal of Geophysical Research: Space Physics*, *119*(2), 909–926. <https://doi.org/10.1002/2013JA019395>
- Liu, J., Angelopoulos, V., Zhou, X.-Z., Runov, A., & Yao, Z. (2013). On the role of pressure and flow perturbations around dipolarizing flux bundles. *Journal of Geophysical Research: Space Physics*, *118*(11), 7104–7118. <https://doi.org/10.1002/2013JA019256>
- Lyons, L. R., Gallardo-Lacourt, B., & Nishimura, Y. (2022). Chapter 2-Auroral structures: Revealing the importance of meso-scale M-I coupling. In Y. Nishimura, O. Verkhoglyadova, Y. Deng, & S.-R. Zhang (Eds.), *Cross-scale coupling and energy transfer in the magnetosphere-ionosphere-thermosphere system* (pp. 65–101). Elsevier. <https://doi.org/10.1016/C2019-0-00526-2>
- Lyons, L. R., Nishimura, Y., Xing, X., Runov, A., Angelopoulos, V., Donovan, E., & Kikuchi, T. (2012). Coupling of dipolarization front flow bursts to substorm expansion phase phenomena within the magnetosphere and ionosphere. *Journal of Geophysical Research*, *117*(A2), A02212. <https://doi.org/10.1029/2011JA017265>
- Mann, I. R., Milling, D. K., & Kale, A. (2023). CARISMA magnetometer network [Dataset]. *University of Alberta*. Retrieved from <https://carisma.ca>
- Mann, I. R., Milling, D. K., Rae, I. J., Ozeke, L. G., Kale, A., Kale, Z. C., et al. (2008). The upgraded CARISMA magnetometer array in the THEMIS era. *Space Science Reviews*, *141*(1–4), 413–451. <https://doi.org/10.1007/s11214-008-9457-6>
- McFadden, J. P., Carlson, C. W., Larson, D., Ludlam, M., Abiad, R., Elliott, B., et al. (2008). The THEMIS ESA plasma instrument and in-flight calibration. *Space Science Reviews*, *141*(1–4), 277–302. <https://doi.org/10.1007/s11214-008-9440-2>
- McPherron, R. L., Russell, C. T., & Aubry, M. A. (1973). Satellite studies of magnetospheric substorms on August 15, 1968, 9, phenomenological model for substorms. *Journal of Geophysical Research*, *78*(16), 3131–3149. <https://doi.org/10.1029/JA078i016p03131>
- Mende, S. B. (2004). THEMIS all sky imager data [Dataset]. *University of California*. Retrieved from <http://themis.ssl.berkeley.edu/themisdata/thg/11/asi/>
- Mende, S. B., Harris, S. E., Frey, H. U., Angelopoulos, V., Russell, C. T., Donovan, E., et al. (2008). The THEMIS array of ground-based observatories for the study of auroral substorms. *Space Science Reviews*, *141*, 357–387. https://doi.org/10.1007/978-0-387-89820-9_16

- Merkin, V. G., Panov, E. V., Sorathia, K., & Ukhorskiy, A. Y. (2019). Contribution of bursty bulk flows to the global dipolarization of the magnetotail during an isolated substorm. *Journal of Geophysical Research: Space Physics*, *124*(11), 8647–8668. <https://doi.org/10.1029/2019JA026872>
- Nagai, T., Fujimoto, M., Saito, Y., Machida, S., Terasawa, T., Nakamura, R., et al. (1998). Structure and dynamics of magnetic reconnection for substorm onsets with Geotail observations. *Journal of Geophysical Research*, *103*(A3), 4419–4440. <https://doi.org/10.1029/97JA02190>
- Nakamura, R., Baumjohann, W., Brittnacher, M. M., Sergeev, V. A., Kubyskhina, M., Mukai, T., & Liou, K. (2001). Flow bursts and auroral activations: Onset timing and foot point location. *Journal of Geophysical Research*, *106*(A6), 10777–10789. <https://doi.org/10.1029/2000JA000249>
- Nakamura, R., Baumjohann, W., Mouikis, C., Kistler, L. M., Runov, A., Volwerk, M., et al. (2004). Spatial scale of high-speed flows in the plasma sheet observed by Cluster. *Geophysical Research Letters*, *31*(9), L09804. <https://doi.org/10.1029/2004GL019558>
- Nakamura, R., Baumjohann, W., Schödel, R., Brittnacher, M., Sergeev, V. A., Kubyskhina, M., et al. (2001). Earthward flow bursts, auroral streamers, and small expansions. *Journal of Geophysical Research*, *106*(A6), 10791–10802. <https://doi.org/10.1029/2000JA000306>
- Newell, P. T., & Gjerloev, J. W. (2011). Evaluation of SuperMAG auroral electrojet indices as indicators of substorms and auroral power. *Journal of Geophysical Research*, *116*(A12), A12211. <https://doi.org/10.1029/2011JA016779>
- Ngwira, C. M., Sibeck, D., Silveira, M. D. V., Georgiou, M., Weygand, J. M., Nishimura, Y., & Hampton, D. (2018). A study of intense local dB/dr variations during two geomagnetic storms. *Space Weather*, *16*(6), 676–693. <https://doi.org/10.1029/2018SW001911>
- Nikitina, L., Trichtchenko, L., & Boteler, D. H. (2016). Assessment of extreme values in geomagnetic and geoelectric field variations for Canada. *Space Weather*, *14*(7), 481–494. <https://doi.org/10.1002/2016SW001386>
- Nishimura, Y., Bortnik, J., Li, W., Thorne, R. M., Lyons, L. R., Angelopoulos, V., et al. (2011). Estimation of magnetic field mapping accuracy using the pulsating aurora-chorus connection. *Geophysical Research Letters*, *38*(14), L14110. <https://doi.org/10.1029/2011GL048281>
- NOAA. (2020). GOES 1–15 space weather instruments, energetic particle sensor (EPS), operational data [Dataset]. *National Centers for Environmental Information, Boulder, Colorado*. Retrieved from <https://www.ncei.noaa.gov/data/goes-space-environment-monitor/access/avg/>
- NOAA. (2023). GOES 1–15 space weather instruments, magnetic fields, science quality data [Dataset]. *National Centers for Environmental Information, Boulder, Colorado*. Retrieved from <https://www.ncei.noaa.gov/data/goes-space-environment-monitor/access/science/mag/>
- Ohtani, S., & Gjerloev, J. W. (2020). Is the substorm current wedge an ensemble of wedgelets? Revisit to midlatitude positive bays. *Journal of Geophysical Research: Space Physics*, *125*(9), e2020JA027902. <https://doi.org/10.1029/2020JA027902>
- Ohtani, S., Singer, H. J., & Mukai, T. (2006). Effects of the fast plasma sheet flow on the geosynchronous magnetic configuration: Geotail and GOES coordinated study. *Journal of Geophysical Research*, *111*(A1), A01204. <https://doi.org/10.1029/2005JA011383>
- Ohtani, S. I., Shay, M. A., & Mukai, T. (2004). Temporal structure of the fast convective flow in the plasma sheet: Comparison between observations and two-fluid simulations. *Journal of Geophysical Research Letters*, *109*(A3), A03210. <https://doi.org/10.1029/2003JA010002>
- Panov, E. V., Baumjohann, W., Nakamura, R., Pritchett, P. L., Weygand, J. M., & Kubyskhina, M. V. (2019). Ionospheric footprints of detached magnetotail interchange heads. *Geophysical Research Letters*, *46*(13), 7237–7247. <https://doi.org/10.1029/2019GL083070>
- Panov, E. V., Baumjohann, W., Nakamura, R., Weygand, J. M., Giles, B. L., Russell, C. T., et al. (2019). Continent-wide R1/R2 current system and ohmic losses by broad dipolarization-injection fronts. *Journal of Geophysical Research: Space Physics*, *124*(6), 4064–4082. <https://doi.org/10.1029/2019JA026521>
- Panov, E. V., Kubyskhina, M. V., Nakamura, R., Wolfgang Baumjohann, W., Angelopoulos, V., Sergeev, V. A., & Petrukovich, A. A. (2013). Oscillatory flow braking in the magnetotail: THEMIS statistics. *Geophysical Research Letters*, *40*(11), 2505–2510. <https://doi.org/10.1002/grl.50407>
- Panov, E. V., Nakamura, R., Baumjohann, W., Angelopoulos, V., Petrukovich, A. A., Retinò, R., et al. (2010). Multiple overshoot and rebound of a bursty bulk flow. *Geophysical Research Letters*, *37*(8), L08103. <https://doi.org/10.1029/2009GL041971>
- Papitashvili, N. E., & King, J. H. (2020). Ground-based magnetometers [Dataset]. *NASA Space Physics Data Facility*. Retrieved from <https://cdaweb.gsfc.nasa.gov/cgi-bin/eval1.cgi>
- Petrukovich, A. A., Sergeev, V. A., Zelenyi, L. M., Mukai, T., Yamamoto, T., Kokubun, S., et al. (1998). Two spacecraft observations of a reconnection pulse during an auroral breakup. *Journal of Geophysical Research*, *103*(A1), 47–59. <https://doi.org/10.1029/97JA02296>
- Rodríguez, J. V. (2014). GOES 13-15 MAGE/PD pitch angles algorithm theoretical basis document, version 1.0. Retrieved from https://www.ngdc.noaa.gov/stp/satellite/goes/doc/MAGEPD_PitchAngles_Processing_ATBD_v1.0.pdf
- Runov, A., Angelopoulos, V., Sitnov, M., Sergeev, V. A., Nakamura, R., Nishimura, Y., et al. (2011). Dipolarization fronts in the magnetotail plasma sheet. *Planetary and Space Science*, *59*(7), 517–525. <https://doi.org/10.1016/j.pss.2010.06.006>
- Runov, A., Angelopoulos, V., Sitnov, M. I., Sergeev, V. A., Bonnell, J., McFadden, J. P., et al. (2009). THEMIS observations of an earthward-propagating dipolarization front. *Geophysical Research Letters*, *36*(14), L14106. <https://doi.org/10.1029/2009GL038980>
- Runov, A., Angelopoulos, V., & Zhou, X.-Z. (2012). Multipoint observations of dipolarization front formation by magnetotail reconnection. *Journal of Geophysical Research*, *117*(A5), A05230. <https://doi.org/10.1029/2011JA017361>
- Russell, C. T. (2004). THEMIS ground-based magnetometer data [Dataset]. *University of California*. Retrieved from <http://themis.ssl.berkeley.edu/data/themis/thg/f2/mag/>
- Russell, C. T., Chi, P. J., Dearborn, D. J., Ge, Y. S., Kuo-Tiong, B., Means, J. D., et al. (2008). THEMIS ground-based magnetometers. *Space Science Reviews*, *141*(1–4), 389–412. <https://doi.org/10.1007/s11214-008-9337-0>
- Sergeev, V. A., Angelopoulos, V., Gosling, J. T., Cattell, C. A., & Russell, C. T. (1996). Detection of localized, plasma-depleted flux tubes or bubbles in the midtail plasma sheet. *Journal of Geophysical Research*, *101*(A5), 10817–10826. <https://doi.org/10.1029/96JA00460>
- Sergeev, V. A., Nikolaev, A. V., Tsyganenko, N. A., Angelopoulos, V., Runov, A. V., Singer, H. J., & Yang, J. (2014). Testing a two-loop pattern of the substorm current wedge (SCW2L). *Journal of Geophysical Research: Space Physics*, *119*(2), 947–963. <https://doi.org/10.1002/2013JA019629>
- Sergeev, V. A., Sauvaud, J. A., Popescu, D., Kovrazhkin, R. A., Liou, K., Newell, P. T., et al. (2000). Multiple-spacecraft observation of a narrow transient plasma jet in the Earth's plasma sheet. *Geophysical Research Letters*, *27*(6), 851–854. <https://doi.org/10.1029/1999GL010729>
- Sergeev, V. A., Sauvaud, J.-A., Popescu, D., Kovrazhkin, R. A., Lutsenko, V. N., Zelenyi, L. M., et al. (2000). Plasma sheet ion injections into the auroral bulge: Correlative study of spacecraft and ground observations. *Journal of Geophysical Research*, *105*(A8), 18465–18482. <https://doi.org/10.1029/1999JA900435>
- Shiokawa, K., Baumjohann, W. W., & Haerendel, G. (1997). Braking of high-speed flows in the near-Earth tail. *Geophysical Research Letters*, *24*(10), 1179–1182. <https://doi.org/10.1029/97GL01062>
- Sibeck, D. G., & Angelopoulos, V. (2008). THEMIS science objectives and mission phases. *Space Science Reviews*, *141*(1–4), 35–59. <https://doi.org/10.1007/s11214-008-9393-5>
- Sillanpää, I., Ganushkina, N. Y., Dubyagin, S., & Rodríguez, J. V. (2017). Electron fluxes at geostationary orbit from GOES MAGED data. *Space Weather*, *15*(12), 1602–1614. <https://doi.org/10.1002/2017SW001698>

- SPEDAS. (2023). Magnetic field models in the SPEDAS GUI [Software]. Retrieved from http://spedas.org/wiki/index.php?title=Magnetic_Field_Models_in_the_SPEDAS_GUI
- Tsurutani, B. T., & Gonzalez, W. D. (1987). The cause of high intensity long duration continuous AE activity (HILDCAAs): Interplanetary Alfvén wave trains. *Planetary and Space Science*, 35(4), 405–412. [https://doi.org/10.1016/0032-0633\(87\)90097-3](https://doi.org/10.1016/0032-0633(87)90097-3)
- Tsurutani, B. T., Gonzalez, W. D., Gonzalez, A. L. C., Tang, F., Arballo, J. K., & Okada, M. (1995). Interplanetary origin of geomagnetic activity in the declining phase of the solar cycle. *Journal of Geophysical Research*, 100(A11), 21717–21733. <https://doi.org/10.1029/95JA01476>
- Tsyganenko, N. A. (1989). A magnetospheric magnetic field model with a warped tail current sheet. *Planetary and Space Science*, 37(1), 5–20. [https://doi.org/10.1016/0032-0633\(89\)90066-4](https://doi.org/10.1016/0032-0633(89)90066-4)
- Tsyganenko, N. A. (1995). Modeling the Earth's magnetospheric magnetic field confined within a realistic magnetopause. *Journal of Geophysical Research*, 100(A4), 5599–5612. <https://doi.org/10.1029/94JA03193>
- Tsyganenko, N. A. (2002a). A model of the near magnetosphere with a dawn-dusk asymmetry, 1. Mathematical structure. *Journal of Geophysical Research*, 107(A8), 1179. <https://doi.org/10.1029/2001JA000219>
- Tsyganenko, N. A. (2002b). A model of the near magnetosphere with a dawn-dusk asymmetry, 2. Parameterization and fitting to observations. *Journal of Geophysical Research*, 107(A8), 1176. <https://doi.org/10.1029/2001JA000220>
- Tsyganenko, N. A. (2022). Empirical magnetosphere models by N. A. Tsyganenko [Software]. *St. Petersburg University*. Retrieved from <https://geo.phys.spbu.ru/tsyganenko/empirical-models/>
- Tsyganenko, N. A., & Andreeva, V. A. (2015a). A forecasting model of the magnetosphere driven by an optimal solar wind coupling function. *Journal of Geophysical Research: Space Physics*, 120, 8401–8425. <https://doi.org/10.1002/2015JA021641>
- Tsyganenko, N. A., & Andreeva, V. A. (2015b). Forecasting models of the magnetosphere driven by optimal solar-wind coupling functions, 2015. Retrieved from http://geo.phys.spbu.ru/tsyganenko/TA15_Model_description.pdf
- Tsyganenko, N. A., & Sitnov, M. I. (2007). Magnetospheric configurations from a high-resolution data-based magnetic field model. *Journal of Geophysical Research*, 112(A6), A06225. <https://doi.org/10.1029/2007JA012260>
- Wei, D., Dunlop, M. W., Yang, J., Dong, X., Yu, Y., & Wang, T. (2021). Intense dB/dt variations driven by near-Earth bursty bulk flows (BBFs): A case study. *Geophysical Research Letters*, 48(4), e2020GL091781. <https://doi.org/10.1029/2020GL091781>
- Weygand, J. M. (2009a). Equivalent ionospheric currents (EICs) derived using the spherical elementary current systems (SECS) technique at 10 s resolution in geographic coordinates. University of California. <https://doi.org/10.21978/P8D62B>
- Weygand, J. M. (2009b). Spherical elementary current (SEC) amplitudes derived using the spherical elementary currents systems (SECS) technique at 10 sec resolution in geographic coordinates. UCLA. <https://doi.org/10.21978/P8PP8X>
- Weygand, J. M., Amm, O., Viljanen, A., Angelopoulos, V., Murr, D., Engebretson, M. J., et al. (2011). Application and validation of the spherical elementary currents systems technique for deriving ionospheric equivalent currents with the North American and Greenland ground magnetometer arrays. *Journal of Geophysical Research*, 116(A3), A03305. <https://doi.org/10.1029/2010JA016177>
- Weygand, J. M., Bortnik, J., Chu, X., Cao, X., Li, J., Aryan, H., & Tian, S. (2022). Magnetosphere-ionosphere coupling between north-south propagating streamers and high-speed earthward flows. *Journal of Geophysical Research: Space Physics*, 127(10), e2022JA030741. <https://doi.org/10.1029/2022JA030741>
- Weygand, J. M., Engebretson, M. J., Pilipenko, V. A., Steinmetz, E. S., Moldwin, M. B., Connors, M. G., et al. (2021). SECS analysis of nighttime magnetic perturbation events observed in Arctic Canada. *Journal of Geophysical Research: Space Physics*, 126(11), e2021JA029839. <https://doi.org/10.1029/2021JA029839>
- Zhou, X.-Z., Angelopoulos, V., Sergeev, V. A., & Runov, A. (2010). Accelerated ions ahead of earthward propagating dipolarization fronts. *Journal of Geophysical Research*, 115(A5), A00I03. <https://doi.org/10.1029/2010JA015481>
- Zhou, X.-Z., Angelopoulos, V., Sergeev, V. A., & Runov, A. (2011). On the nature of precursor flows upstream of advancing dipolarization fronts. *Journal of Geophysical Research*, 116, A03222. <https://doi.org/10.1029/2010JA016165>
- Zou, Y., Dowell, C., Ferdousi, B., Lyons, L. R., & Liu, J. (2022). Auroral drivers of large dB/dt during geomagnetic storms. *Space Weather*, 20(11), e2022SW003121. <https://doi.org/10.1029/2022SW003121>